

SUPPLEMENTARY INFORMATION

Selective oxidation of alkyl and aryl glyceryl monoethers catalyzed by an engineered and immobilised glycerol dehydrogenase

Susana Velasco-Lozano,^[a] Maite Roca,^[b] Alejandro Leal-Duaso,^[a] José A. Mayoral,^[a,c] Elisabet Pires,^{*,[a,e]} Vicent Moliner^{*,[b]} and Fernando López-Gallego.^{*,[a,c,d,e]}

^[a]Catálisis Heterogénea en Síntesis Orgánicas Selectivas, Instituto de Síntesis Química y Catálisis Homogénea (ISQCH-CSIC), University of Zaragoza, Pedro Cerbuna, 12, 50009, Zaragoza, Spain.

^[b]Departament de Química Física i Analítica, Universitat Jaume I, 12071 Castelló, Spain.

^[c]Depto. de Química Orgánica. Facultad de Ciencias. University of Zaragoza, Pedro Cerbuna, 12, 50009, Zaragoza, Spain.

^[d]Heterogeneous biocatalysis laboratory. Center for Cooperative Research in Biomaterials (CIC biomaGUNE), Basque Research and Technology Alliance (BRTA), Paseo de Miramón 182, 20014, Donostia San Sebastián, Spain.

^[e]IKERBASQUE, Basque Foundation for Science. Maria Diaz de Haro 3, 48013 Bilbao, Spain.

Content

1. Computational studies	3
1.1. Computation methods.....	3
1.1.1 System setup and molecular dynamic simulations	3
1.1.2 QM/MM simulations and Free Energy Profiles	4
1.2 Computational results	5
1.2.1 Analysis of the MM MD simulations	5
1.2.2 Free Energy Profiles	6
2. Supplementary figures	10
Figure S1. The SDS-PAGE of the expression and purification of the BsGlyDH mutants.	10
Figure S2. Schematic representation of the active site of BsGlyDH.	11
Figure S3. Time evolution of the protein backbone RMSD	12
Figure S4. Time evolution of the distance between H atom of glycerol and the oxygen atoms.....	13
Figure S5. M06-2X:PM3/MM PMFs + ZPE corrections for the wild-type system with glycerol ..	14
Figure S6. (A) M06-2X(6-31+G(d,p))/MM PES for mechanism 1 of the wild-type BsGlyDH with glycerol substrate.....	15
Figure S7. Specific activity of different BsGlyDH mutants	16
Figure S8. Structural multi-sequence alignment of glycerol polyol dehydrogenases.....	17
Figure S9. Structural alignment of BsGlyDH (PDB ID: 1JQ5, green) with GlyDHs (A) and archeal glycerol 1-phosphate dehydrogenase (B).....	18

Figure S10. Effect of the solvent accessible area in the activity of BsGlyDH variants.....	19
Figure S11. Kinetic parameters of BsGlyDH-WT.	20
Figure S12. Kinetic parameters of BsGlyDH-L252A.....	21
Figure S13. Kinetic parameters of BsGlyDH variants with NAD ⁺	22
Figure S14. pH profile of GlyDH WT and mutant L252A.....	23
Figure S15. M06-2X/6-31+G(d,p):PM3/MM PMFs with ZPE corrections for mechanism 2 of the wild-type BsGlyDH system with <i>R</i> -1c.....	24
Figure S16. M06-2X/6-31+G(d,p):PM3/MM PMFs with ZPE corrections for mechanism 2 of the BsGlyDH-L252A system with glycerol.....	25
Figure S17. Average interaction energies (electrostatic plus Lennard-Jones) by residue between the enzyme and the substrates over 1000 structures of the QM/MM MD simulations on the reactant state.....	26
Figure S18. Average electrostatic (Elec) and Lennard-Jones (LJ) contributions to the interaction energy between the key residues and the substrates over 1000 structures of the QM/MM MD simulations on the reactant state.....	27
Figure S19. ¹ H NMR of the reaction mixture of the oxidation of 1c.....	28
Figure S20. ¹ H NMR of the pure glyceryl monoether 1c.....	28
Figure S21. ¹³ C NMR (APT) of the reaction mixture of the oxidation of 1c.....	29
Figure S22. ¹³ C NMR (APT) of the pure glyceryl monoether 1c.....	29
Figure S23. GC-MS analysis of sample: Negative reaction control (without enzyme).....	30
Figure S24. GC-MS analysis. Sample: Enzymatic reaction, remnant substrate.....	31
Figure S25. GC-MS analysis. Sample: Enzymatic reaction: oxidised product of.....	31
Figure S26. GC-MS analysis. Sample: Negative reaction control (without enzyme): acetylated substrate.....	32
Figure S27. GC-MS analysis. Sample: Enzymatic reaction: acetylated substrate 1c.....	32
Figure S28. GC-MS analysis. Sample: Enzymatic reaction: acetylated.....	33
Figure S29. Chiral HPLC chromatogram of standard <i>rac</i> -1h.....	33
Figure S30. Chiral HPLC chromatogram of standard <i>R</i> -1h.....	34
Figure S31. Chiral HPLC chromatogram of standard <i>S</i> -1h.....	34
Figure S32. Chiral HPLC chromatograms of negative reaction control mixture at 72 h.....	35
Figure S33. Chiral HPLC chromatograms of enzymatic reaction samples of <i>rac</i> -1h at 72 h.....	35
Figure S34. Inhibition of BsGlyDH enzymes by DHA.....	36
Figure S35. Oxidation of 1c catalyzed by immobilised GlyDH-L252-AG-Co ²⁺ and different immobilised NADH oxidases.....	36
Figure S36. Batch reactor.....	37

3. Supplementary tables.....	38
Table S1. Glyceryl ethers employed as substrates in this work.	38
Table S2. Design of mutated positions in the BsGlyDH primary sequence.	39
Table S3. Activity of different glycerol dehydrogenases towards glycerol ethers.	40
Table S4. BsGlyDH mutations to expand the binding pocket.	41
Table S5. Gibbs free energies calculated with QM/MM	42
Table S6. Immobilization parameters of BsGlyDH-L252A.	43

1. Computational studies

1.1. Computation methods

1.1.1 System setup and molecular dynamic simulations

The wild-type system was built using the crystal structures with access codes 1JQ5 and 1JQA.¹ Both structures were superimposed using PyMOL software² and the glycerol substrate from 1JQA structure was introduced into the active site of the 1JQ5 structure that contains NAD⁺ and Zn²⁺. At the crystal structure,¹ the glycerol presents two different conformations (major and minor orientations). Major orientation was selected as the starting point because glycerol overlaps with NAD⁺ cofactor in the minor orientation. The L252A mutant was obtained by replacing leucine residue 252 by alanine residue, and the glycerol was also introduced into the active site in its major orientation. On the other hand, the reaction was also studied using another substrate where the hydrogen atom bound to O3 atom of glycerol was replaced by an ethyl group (3-Ethoxypropan-1,2-diol **1c**), for both, wild-type and L252A mutant. Then, all the systems (wild-type BsGlyDH with glycerol, *S*-**1c** and *R*-**1c** enantiomers, BsGlyDH-L252A mutant with glycerol, *S*-**1c** and *R*-**1c** enantiomers and BsGlyDH-D123N mutant with glycerol) were built up to perform the computational study.

The PROPKA3.0 program³⁻⁶ was used to estimate the pK_a values of the titratable protein residues to verify their protonation states at a pH of 7 and missing hydrogen atoms were added using the tLEaP module⁷ of AmberTools17 package.⁸ According to the results, all the lysine and arginine residues are positively charged and all the aspartate and glutamate residues are negatively charged, while the rest of the residues are neutral. All protein force field parameters are taken from the AMBER ff14SB force field.⁸ Glycerol was parametrised using the Antechamber program⁹ from the AmberTools17 package,⁸ based on the general amber force field,¹⁰ while the parameters for NAD⁺ were taken from FF94 and FF99 force fields.^{11, 12} The coordination of Zn²⁺ ion was parametrised using the Metal Center Parameter Builder (MCPB) program developed by Martin Peters at the

University of Florida in the lab of Kenneth Merz Jr.^{13, 14} All the systems were solvated by a box of TIP3P water molecules¹⁵ with a buffer region of at least 13 Å from any protein or substrate atom to the limits of the box and were also neutralised adding 10 Na⁺ counterions by tLEaP module⁷ from AmberTools17 package.

Firstly, all the systems were minimised using 5000 steps of steepest descent method followed by 5000 steps of conjugate gradient minimization for a maximum of 10,000 minimization steps. After heating the systems to 303 K during a 500 ps molecular dynamic (MD) simulation, 1 ns of NPT MD simulation at 303 K and 1 bar was performed. Finally, a 100 ns MD production was performed using the NVT ensemble. A time step of 1 fs was employed and the SHAKE algorithm^{16, 17} was used to constraint all the bonds involving hydrogens. Long-range electrostatic interactions were treated by the particle mesh Ewald (PME) method¹⁷⁻¹⁹ and short-range non-bonded interactions were truncated using a cutoff of 10 Å in periodic boundary conditions. Langevin thermostat²⁰ and Berendsen barostat²¹ were used to control temperature and pressure, respectively.

1.1.2 QM/MM simulations and Free Energy Profiles

The wild-type system with glycerol substrate was used in order to elucidate the reaction mechanism. The two different conformations found along the MM MD simulations were taken to perform quantum mechanics/molecular mechanics (QM/MM) MD simulations. A total of 1 ns of QM/MM MD simulations was performed. The QM region depends on the reaction mechanism to be studied (Figure 2). For mechanism 1, the QM region consists of glycerol, part of NAD⁺ cofactor, Zn²⁺ ion, the side chains of the coordination sphere of Zn²⁺ and a water molecule, whereas for mechanism 2, the water molecule is replaced by the side chain of the Asp123 residue (Figure S2). Figure S2 shows the two different QM regions for both mechanisms. The QM region consists of 78 and 82 atoms for mechanism 1 and mechanism 2, respectively. The QM atoms were described first by means of PM3²², with the zinc biological (ZnB) parameter set,²³ and later with the Minnesota Density Functional M06-2X,²⁴ with the standard 6-31+G(d,p) basis set. The rest of protein system and the solvent water molecules were described by AMBER and TIP3P force fields, respectively, implemented in fDynamo library.^{25, 26} To saturate the valence of the QM/MM frontier, the link atom procedure was used.²⁷ A switch function with a cutoff distance in the range of 10-14 Å was used to treat the nonbonding interactions.

Once the system was equilibrated, hybrid QM/MM potential energy surface (PES) explorations and transition state (TS) structure location and characterization were carried out, by means of a micro-macro iteration optimization algorithm.²⁸ Once the TS structures were localised, these structures were used as starting configurations to obtain the potential of mean force (PMF). The umbrella sampling approach²⁹ was used to constraint the system, applying a force constant of $2500 \text{ kJ} \cdot \text{mol}^{-1} \text{ \AA}^{-2}$ to the selected distinguished reaction coordinates. The full probability distribution was obtained by means of the weighted histogram analysis method (WHAM)³⁰ implemented in fDynamo library. For both mechanisms, the selected distinguished reaction coordinates were the antisymmetric combination of the bond breaking and bond forming distances in each step. The simulation windows of the PMFs consisted of 10 ps of equilibration and 20 ps of production, with a time step of 0.5 fs. Mechanism 1 and 2 were tested for wild-type BsGlyDH with glycerol to computationally decipher the mechanism, performing PES explorations, TS structures localizations and PMFs. For the rest of the systems, once minimised and equilibrated, only the most plausible mechanism (mechanism 2) was studied following the same procedure abovementioned.

Because of the large number of structures that must be evaluated during free energy calculations, QM/MM MD simulations are usually restricted to the use of semiempirical Hamiltonians. In order to correct the PM3/MM PMFs using a higher level method to describe the QM region, an interpolated correction scheme developed in our laboratory has been applied.³¹ The M06-2X density functional with the 6-31+G(d,p) basis set was selected as the high level method using Gaussian09 program.³² A minimization process was performed along the PMF and single point energy calculations at the high level method (M06-2X/6-31+G(d,p)) and a low level method (PM3) of the minimised structures along the PMF were performed.

1.2 Computational results

1.2.1 Analysis of the MM MD simulations

The root-mean-square-deviation (RMSD) of those atoms belonging to the protein backbone of all the systems is shown in Figure S3. According to the RMSD evolution along the MD simulations (Figure S3), the systems can be considered equilibrated. The time evolution of the distance between the proton atom of glycerol (H in Figure 2 and Figure S2) and the oxygen atoms of Asp123 residue along the MD simulations is also obtained. Figure S4 displays the distance between H atom of glycerol and the oxygen atoms of Asp123 residue of wild-type BsGlyDH, showing two configurations of the substrate that lead to the two different reaction mechanism proposed in Figure 2. One conformation orients the glycerol towards a water molecule that acts as a base to abstract

the proton from the hydroxyl group linked to the C2 atom of glycerol (Mechanism 1 in Figure 2). Whereas, the other conformation allows establishing a hydrogen bond between the hydroxyl group of C2 atom from glycerol and one oxygen atom of the carboxylic Asp123 residue (Mechanism 2 in Figure 2).

In the case of the D123N mutant with glycerol, the RMSD evolution along the MD simulations is also displayed in Figure S3. Asparagine residue establishes hydrogen bond interactions with glycerol and other residues and no water molecules enter into the active site. Then, there are no candidates to act as a base to abstract the proton from glycerol and, thus, as experimentally observed, this mutant is not active.

1.2.2 Free Energy Profiles

Mechanism 1 was studied starting from the wild-type structure with glycerol. From the equilibrated structure with the H atom of glycerol oriented to a water molecule, a PES of the first step was explored and the PMF was performed. A total of 131 simulation windows were performed by changing the distinguished reaction coordinate, the bond breaking ($d(O2(\text{glycerol}), H(\text{glycerol}))$) and bond forming ($d(H(\text{glycerol}), O_{\text{wat}})$) distances, in 0.02 \AA . After that, the PMF for the second step was performed where the distinguished reaction coordinate used was the antisymmetric combination of the bond breaking ($d(C2(\text{glycerol}), H2(\text{glycerol}))$) and bond forming ($d(H2(\text{glycerol}), C4(\text{NAD}^+))$) distances. A total of 151 simulation windows were simulated. Corrections to the PMF were applied using the M06-2X/6-31+G(d,p) density functional to describe the QM region. Moreover, zero point energy (ZPE) corrections to the activation free energy barrier were also computed. From a trajectory with the reaction coordinate constrained on the reactants and the highest energy TS, a set of 10 TS and reactant structures were localised and characterised to compute the ZPE correction to the activation free energy. Finally, a free energy barrier of $57.6 \text{ kcal}\cdot\text{mol}^{-1}$ was obtained (Figure S5) and only one transition state structure (labeled as TS in Figure S5) was localized and characterized for the hydride transfer reaction. A very high barrier being not compatible for an enzymatic reaction. Furthermore, a two dimensional PES using a higher level (M06-2X(6-31+G(d,p))/MM) was performed to sustain this result (Figure S6A). From these results, mechanism 1 can be ruled out.

Starting from the configuration in which H atom of glycerol is establishing hydrogen bond interaction with the Asp123 residue, mechanism 2 was studied. Firstly, the PES of the first step was explored, a TS structure was localised and characterised and from this structure the PMF was performed. The antisymmetric combination of the bond breaking ($d(O2(\text{glycerol}), H(\text{glycerol}))$) and

bond forming ($d(\text{H}(\text{glycerol}), \text{OD1}(\text{Asp123}))$) distances was used as the distinguished reaction coordinate and a total of 111 simulation windows were performed to obtain the PMF. Afterwards, the second step was explored following the same procedure where the reaction coordinate used was the antisymmetric combination of the bond breaking ($d(\text{C2}(\text{glycerol}), \text{H2}(\text{glycerol}))$) and bond forming ($d(\text{H2}(\text{glycerol}), \text{C4}(\text{NAD}^+))$) distances and 161 simulation windows were carried out. To verify that is a stepwise mechanism, two dimensional M06-2X(6-31+G(d,p))/MM PES exploration was carried out using the two antisymmetric combinations of the bond breaking and bond forming distances of the two steps (Figure S6B). Finally, the PMF was corrected using the M06-2X/6-31+G(d,p) method to describe the QM region and adding ZPE corrections. Figure S5 shows the M06-2X/6-31+G(d,p):PM3/MM PMF and ZPE correction of this mechanism (blue line). The free energy barrier obtained, $17.1 \text{ kcal}\cdot\text{mol}^{-1}$, is in agreement with the experimentally derived value (k_{cat} of 237 min^{-1} corresponding to a free energy barrier of $16.9 \text{ kcal}\cdot\text{mol}^{-1}$ at a temperature of 303 K). Thus, one could conclude that this reaction mechanism is a viable mechanism for the enzymatic reaction.

To endorse this conclusion, Asp123 was mutated to an asparagine residue (BsGlyDH-D123N) and MM MD simulations were performed. According to the computational analyses of this variant, we found no base close to the H proton of glycerol to be abstracted, in consequence, this system is not reactive as observed experimentally (Figure S7) and the computational mechanistic study is not performed.

Finally, in order to computationally assess the enantiopreference of **1c** substrate in both enzymes, wild-type BsGlyDH and BsGlyDH-L252A, we obtained M06-2X/6-31+6G(d,p):PM3/MM PMFs for both **1c** enantiomers (*S* and *R*) using wild-type BsGlyDH (Figure S15) and BsGlyDH-L252A (Figure 4). Moreover, the M06-2X/6-31+6G(d,p):PM3/MM PMF was also performed for the BsGlyDH-L252A system with glycerol (Figure S16). All these PMFs were obtained following the same procedure as described before for the wild-type BsGlyDH with glycerol.

In order to analyse the interactions of the key residues that form the cavity (V131, Y142 and L252) with the substrate, the total interaction energy (electrostatic plus Lennard-Jones energies) between residues and the substrate were computed as an average over 1000 structures of the equilibration QM/MM MD simulation (Figure S17) on the reactant state. These calculations were performed for the WT and L252A mutant with glycerol and *S*-**1c** substrates. In all the structures, the interaction energies between V131, Y142 and L252 residues and the respective substrates are small and negative. This means that these residues stabilize the reactant state in both enzymes, although at

low extent. The electrostatic and Lennard-Jones contributions for the key residues are shown in Figure S18. In these residues, and especially residue 252, the Lennard-Jones energy is much higher than the electrostatic energy, thus confirming that the role of these residues can be explained based on just steric factors.

References

1. S. N. Ruzheinikov, J. Burke, S. Sedelnikova, P. J. Baker, R. Taylor, P. A. Bullough, N. M. Muir, M. G. Gore and D. W. Rice, *Structure*, 2001, **9**, 789-802.
2. www.pymol.org.
3. H. Li, A. D. Robertson and J. H. Jensen, *Proteins*, 2005, **61**, 704-721.
4. D. C. Bas, D. M. Rogers and J. H. Jensen, *Proteins*, 2008, **73**, 765-783.
5. M. H. M. Olsson, C. R. Sondergaard, M. Rostkowski and J. H. Jensen, *J. Chem. Theory Comput.*, 2011, **7**, 525-537.
6. C. R. Sondergaard, M. H. M. Olsson, M. Rostkowski and J. H. Jensen, *J. Chem. Theory Comput.*, 2011, **7**, 2284-2295.
7. C. E. A. F. Schafmeister, W. S. Ross and V. Romanovski, *University of California, San Francisco*, 1995.
8. D. A. Case, D. S. Cerutti, T. E. Cheatham III, T. A. Darden, R. E. Duke, T. J. Giese, H. Gohlke, A. W. Goetz, N. Homeyer, S. Izadi, A. Kovalenko, T. S. Lee, S. LeGrand, P. Li, C. Lin, J. Liu, T. Luchko, R. Luo, D. J. Mermelstein, K. M. Merz, G. Monard, H. Nguyen, I. Omelyan, A. Onufriev, F. Pan, R. Qi, D. R. Roe, A. Roitberg, C. Sagui, C. L. Simmerling, W. M. Botello-Smith, J. Swails, R. C. Walker, J. Wang, R. M. Wolf, X. Wu, L. Xiao, D. M. York and P. A. Kollman, *University of California, San Francisco*, 2017.
9. J. Wang, W. Wang, P. A. Kollman and D. A. Case, *J. Mol. Graph. Model.*, 2006, **25**, 247-260.
10. J. M. Wang, R. M. Wolf, J. W. Caldwell, P. A. Kollman and D. A. Case, *J. Comput. Chem.*, 2004, **25**, 1157-1174.
11. R. C. Walker, M. M. de Souza, I. P. Mercer, I. R. Gould and D. R. Klug, *J. Phys. Chem. B*, 2002, **106**, 11658-11665.
12. J. J. Pavelites, J. Gao, P. A. Bash and A. D. Mackerell Jr., *J. Comput. Chem.*, 1997, **18**, 221-239.
13. M. B. Peters, Y. Yang, B. Wang, L. Füsti-Molnár, M. N. Weaver and K. M. Merz, *J. Chem. Theory Comput.*, 2010, **6**, 2935-2947.
14. P. Li and K. M. Merz, *J. Chem. Inf. Model.*, 2016, **56**, 599-604.
15. W. L. Jorgensen, J. Chandrasekhar, J. D. Madura, R. W. Impey and M. L. Klein, *J. Chem. Phys.*, 1983, **79**, 926-935.
16. J. P. Ryckaert, G. Ciccotti and H. J. C. Berendsen, *J. Comput. Phys.*, 1977, **23**, 327-341.
17. T. Darden, D. York and L. Pedersen, *J. Chem. Phys.*, 1993, **98**, 10089-10092.
18. D. M. York, T. A. Darden and L. G. Pedersen, *J. Chem. Phys.*, 1993, **99**, 8345-8348.
19. U. Essmann, L. Perera, M. L. Berkowitz, T. Darden, H. Lee and L. G. Pedersen, *J. Chem. Phys.*, 1995, **103**, 8577-8593.
20. G. S. Grest and K. Kremer, *Phys. Rev. A*, 1986, **33**, 3628-3631.
21. H. J. C. Berendsen, J. P. M. Postma, W. F. Vangunsteren, A. Dinola and J. R. Haak, *J. Chem. Phys.*, 1984, **81**, 3684-3690.
22. J. J. P. Stewart, *J. Comput. Chem.*, 1989, **10**, 209-220.

23. E. N. Brothers, D. Suarez, D. W. Deerfield and K. M. Merz, *J. Comput. Chem.*, 2004, **25**, 1677-1692.
24. Y. Zhao and D. G. Truhlar, *Theor. Chem. Acc.*, 2008, **120**, 215-241.
25. M. J. Field, M. Albe, C. Bret, F. Proust-De Martin and A. Thomas, *J. Comput. Chem.*, 2000, **21**, 1088-1100.
26. A. Krzemieska, P. Paneth, V. Moliner and K. Swiderek, *J. Phys. Chem. B*, 2015, **119**, 917-927.
27. M. J. Field, P. A. Bash and M. Karplus, *J. Comput. Chem.*, 1990, **11**, 700-733.
28. S. Marti, V. Moliner and I. Tunon, *J. Chem. Theory Comput.*, 2005, **1**, 1008-1016.
29. G. M. Torrie and J. P. Valleau, *J. Comput. Phys.*, 1977, **23**, 187-199.
30. S. Kumar, D. Bouzida, R. H. Swendsen, P. A. Kollman and J. M. Rosenberg, *J. Comput. Chem.*, 1992, **13**, 1011-1021.
31. J. J. Ruiz-Pernia, E. Silla, I. Tunon, S. Marti and V. Moliner, *J. Phys. Chem. B*, 2004, **108**, 8427-8433.
32. M. J. Frisch, G. W. Trucks, H. B. Schlegel, G. E. Scuseria, M. A. Robb, J. R. Cheeseman, G. Scalmani, V. Barone, B. Mennucci, G. A. Petersson, H. Nakatsuji, M. Caricato, X. Li, H. P. Hratchian, A. F. Izmaylov, J. Bloino, G. Zheng, J. L. Sonnenberg, M. Hada, M. Ehara, K. Toyota, R. Fukuda, J. Hasegawa, M. Ishida, T. Nakajima, Y. Honda, O. Kitao, H. Nakai, T. Vreven, J. A. Montgomery Jr., J. E. Peralta, F. Ogliaro, M. J. Bearpark, J. J. Heyd, E. N. Brothers, K. N. Kudin, V. N. Staroverov, R. Kobayashi, J. Normand, K. Raghavachari, A. P. Rendell, J. C. Burant, S. S. Iyengar, J. Tomasi, M. Cossi, N. Rega, J. M. Millam, M. Klene, J. E. Knox, J. B. Cross, V. Bakken, C. Adamo, J. Jaramillo, R. Gomperts, R. E. Stratmann, O. Yazyev, A. J. Austin, R. Cammi, C. Pomelli, J. W. Ochterski, R. L. Martin, K. Morokuma, V. G. Zakrzewski, G. A. Voth, P. Salvador, J. J. Dannenberg, S. Dapprich, A. D. Daniels, Ö. Farkas, J. B. Foresman, J. V. Ortiz, J. Cioslowski and D. J. Fox, *Wallingford, CT*, 2009.

2. Supplementary figures

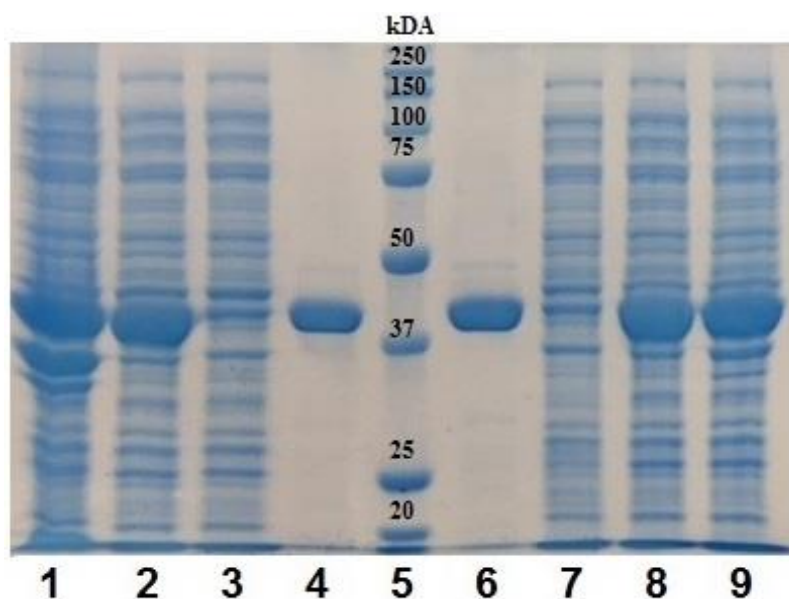


Figure S1. The SDS-PAGE of the expression and purification of the BsGlyDH mutants. BsGlyDH-L252A (1-4) and BsGlyDH-V131A (6-9). 5: Molecular weight marker (BioRad Precision Plus Protein All Blue Standard). 1 and 9: Crude extracts. 2 and 8: Soluble fraction after cell disruption by sonication. 3 and 7: Elution fraction. 4 and 6: Pure enzymes (BsGlyDH-L252A and BsGlyDH-V131A, respectively).

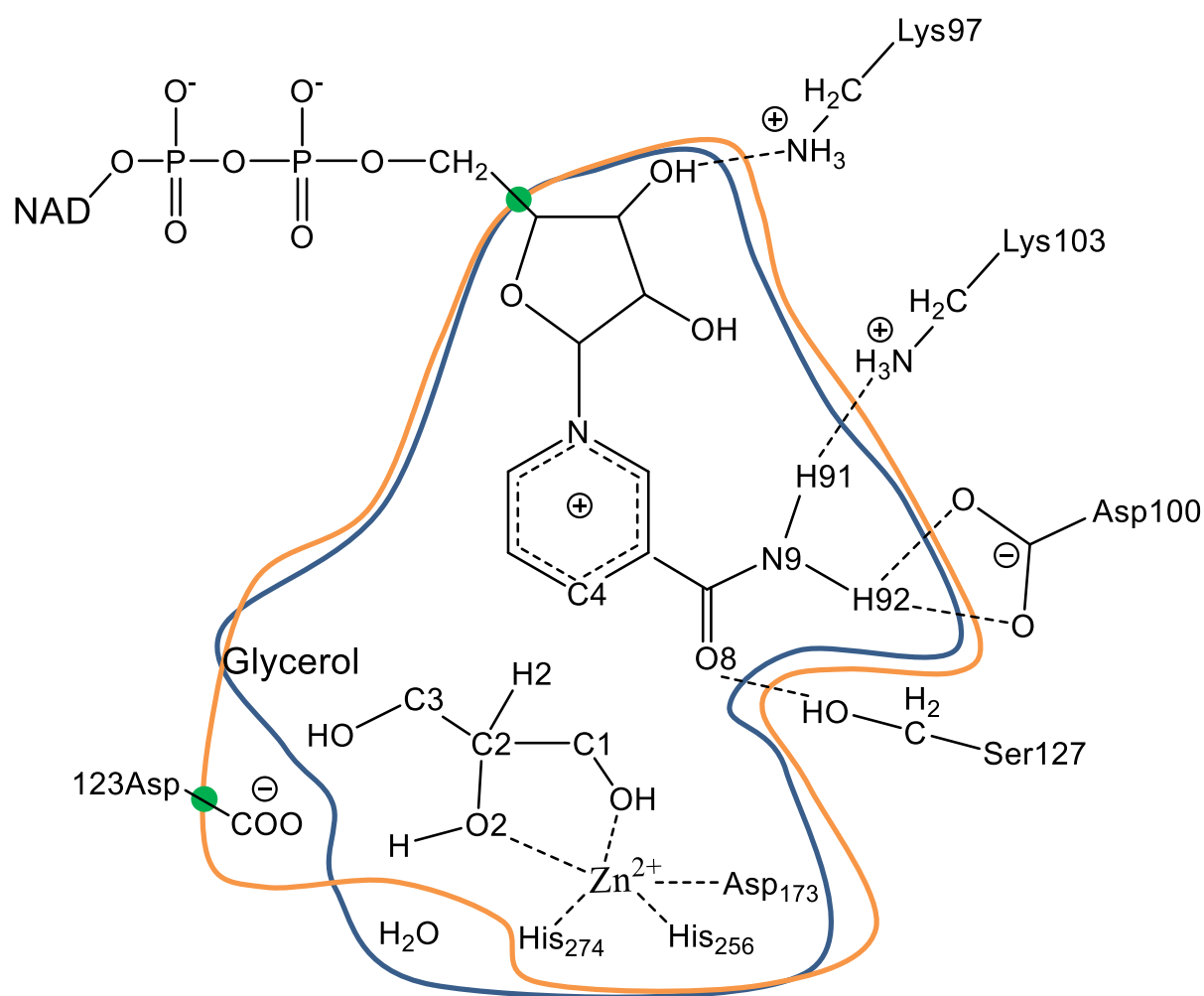


Figure S2. Schematic representation of the active site of BsGlyDH. The regions described quantum mechanically are inside the blue and orange curves for the study of mechanism 1 and mechanism 2, respectively. The link atoms are displayed as green balls.

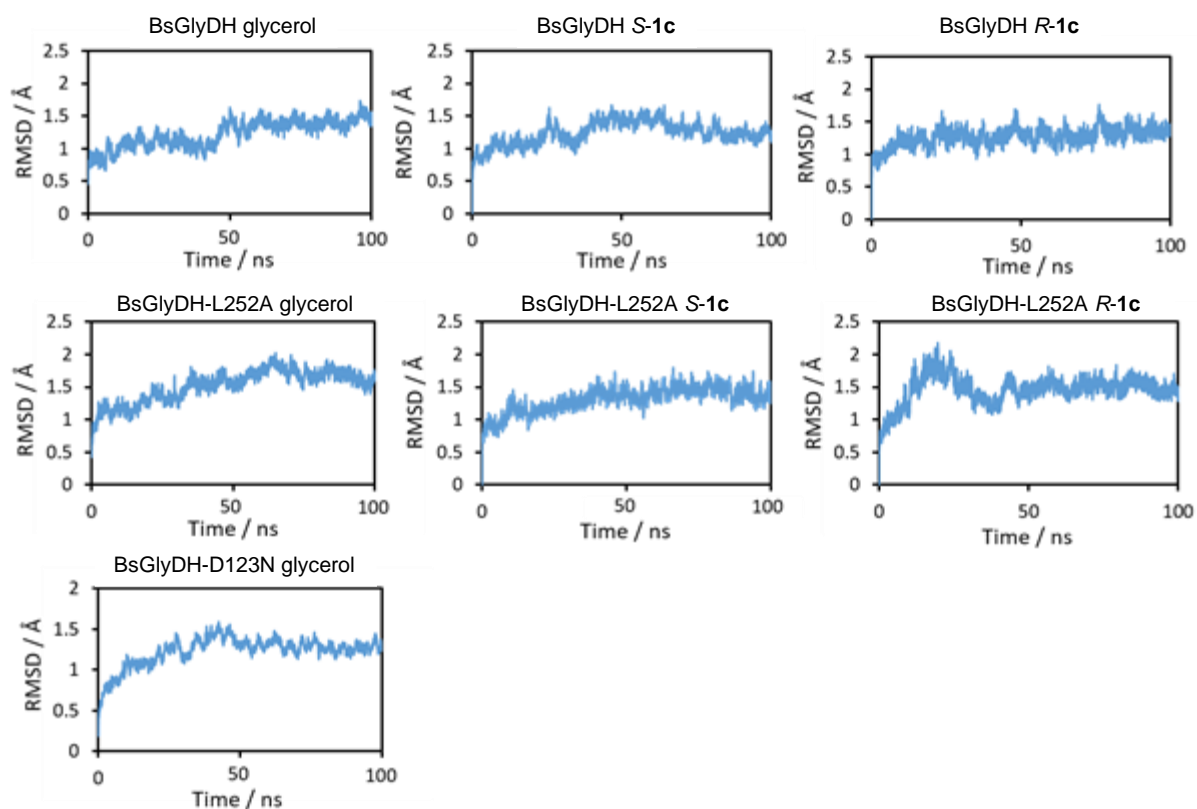


Figure S3. Time evolution of the protein backbone RMSD (in Å) along 100 ns (X-axis) MD simulation of all the studied systems with respect to the first frame of the MD simulation.

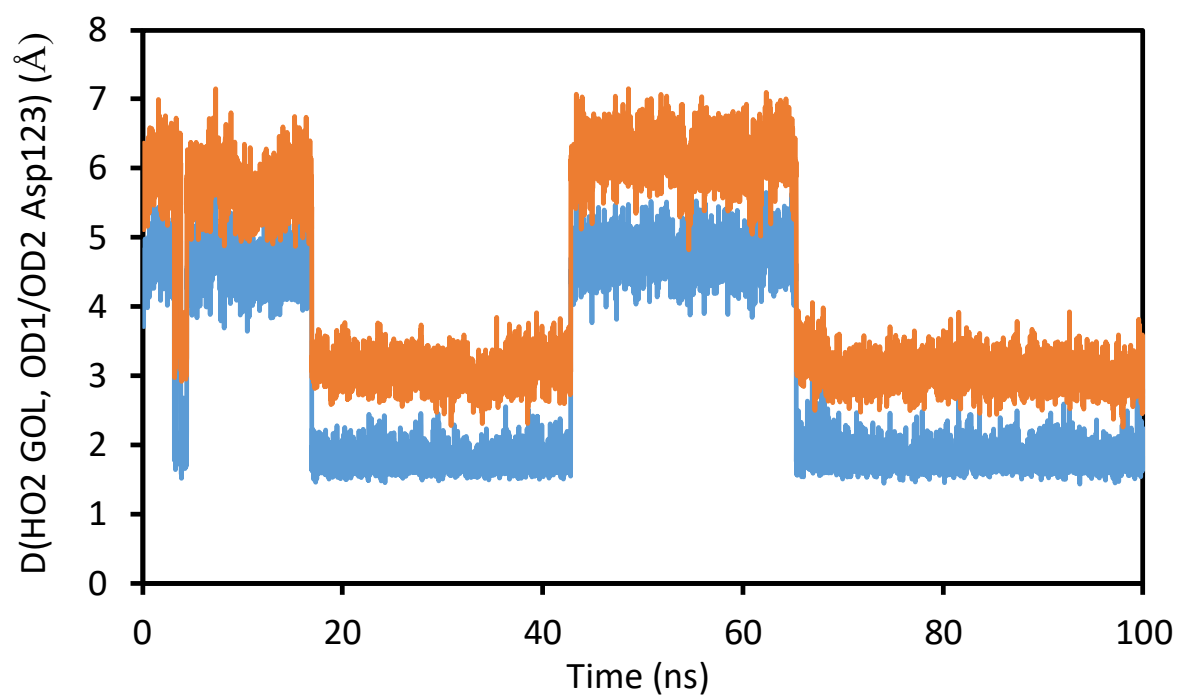


Figure S4. Time evolution of the distance between H atom of glycerol and the oxygen atoms of the carboxylic group of Asp123 residue along 100 ns MD simulation of wild-type system.

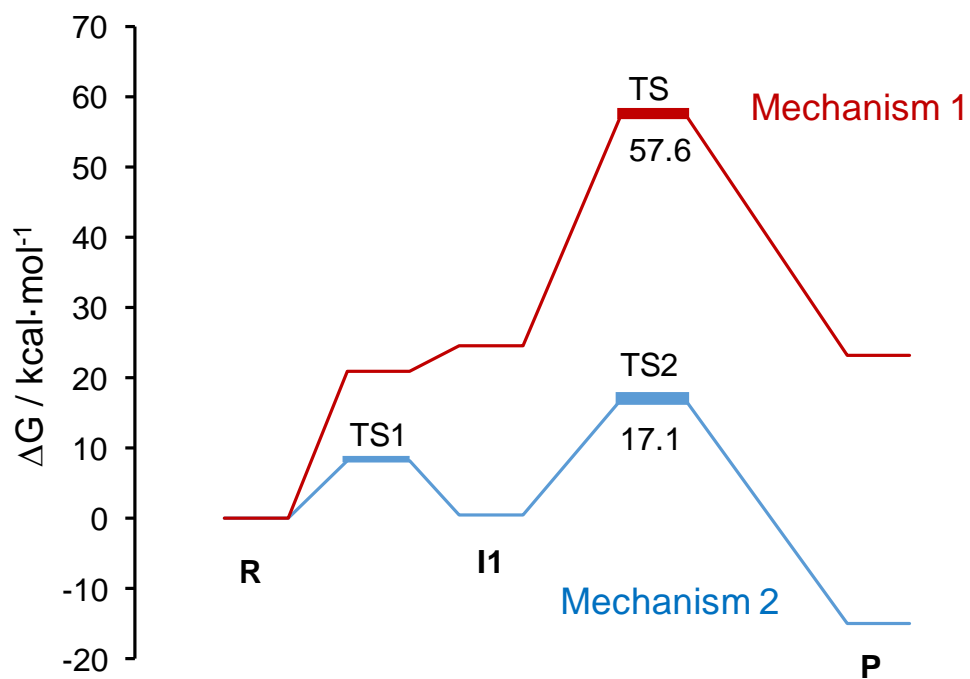


Figure S5. M06-2X:PM3/MM PMFs + ZPE corrections for the wild-type system with glycerol following the mechanism 1 (red) and 2 (blue). R: glycerol / TS1: Transition state 1 for mechanism 2 / I1:alkoxide intermediate / TS2: Transition state 2 for mechanism 2 / TS: Transition state for mechanism 1 / P: Dihydroxyacetone

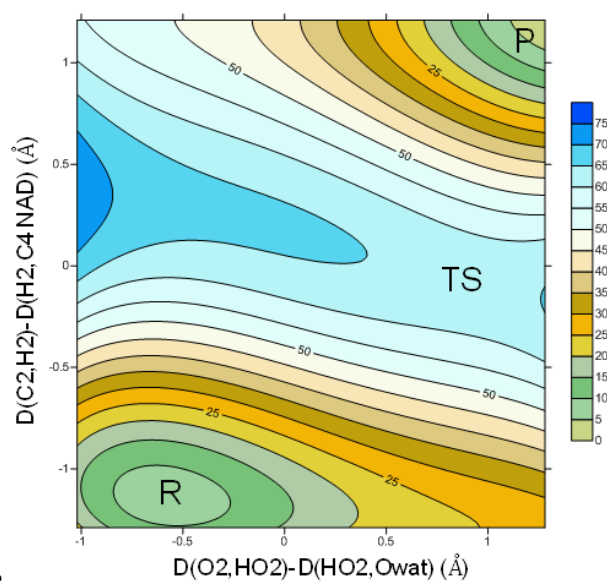
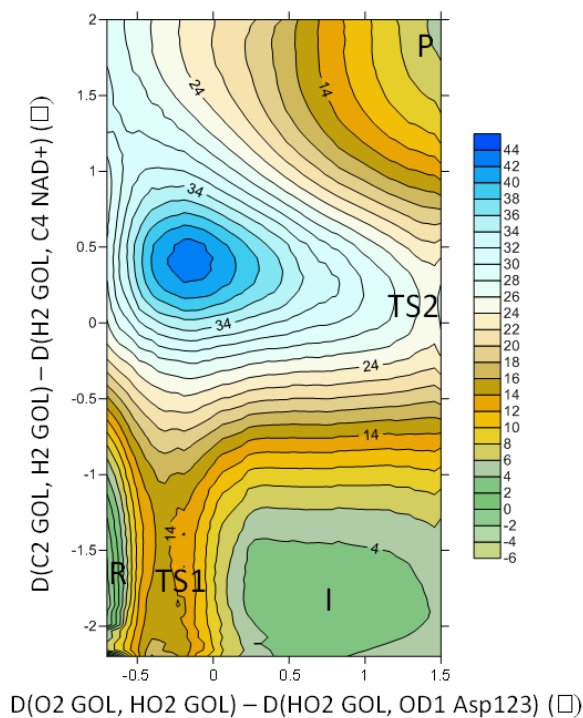
A**B**

Figure S6. (A) M06-2X(6-31+G(d,p))/MM PES for mechanism 1 of the wild-type BsGlyDH with glycerol substrate. The energies are in kcal·mol⁻¹. (B) M06-2X(6-31+G(d,p))/MM PES for mechanism 2 of the wild-type BsGlyDH with glycerol substrate. The energies are in kcal·mol⁻¹. R: glycerol / TS1: Transition state 1 / I:alkoxide intermediate / TS2: Transition state 2 / P: Dihydroxyacetone

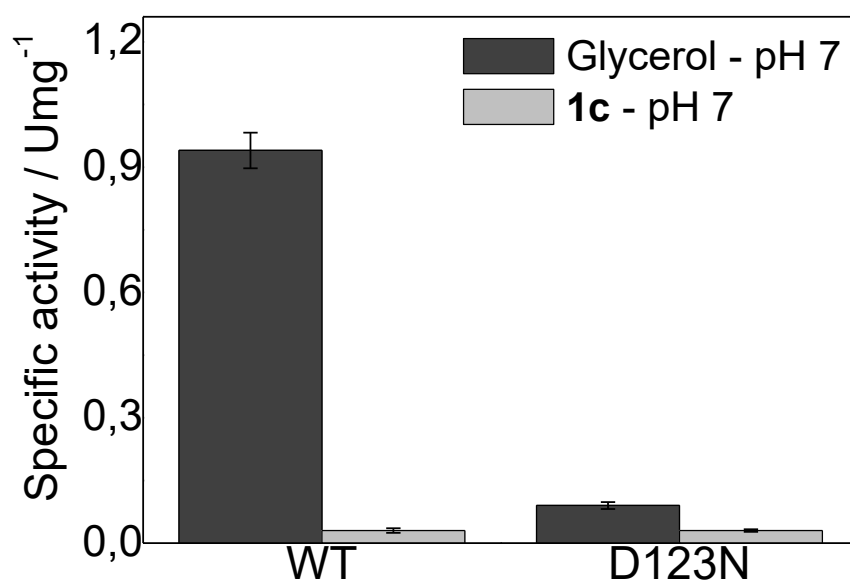


Figure S7. Specific activity of different BsGlyDH mutants at position 123 for the oxidation of different substrates at pH 7.

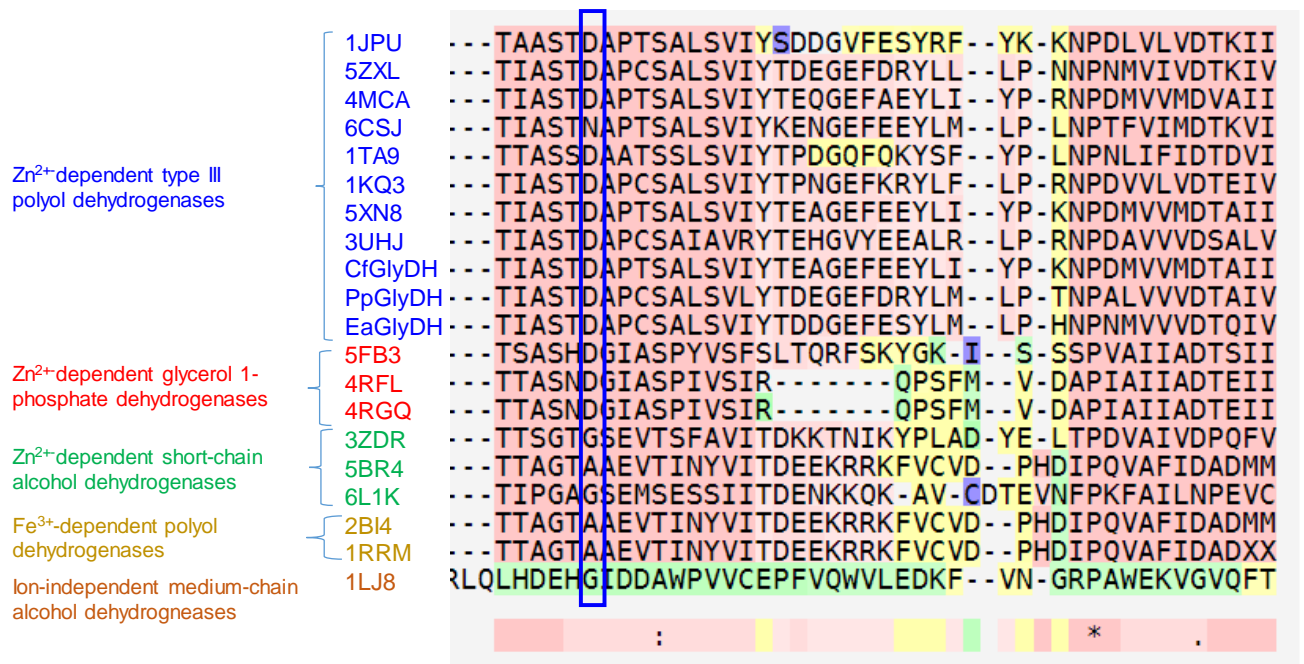


Figure S8. Structural multi-sequence alignment of glycerol polyol dehydrogenases. The aligned sequences are; type-III Zn²⁺-dependent polyol dehydrogenases from *Geobacillus stearothermophilus* (PDB ID: 1JPU), from *Escherichia coli* K-12 (PDB ID: 5ZXL), from *Serratia plymuthica* A30 (PDB ID: 4MCA), from *Bacillus coagulans* (PDB ID: 6CSJ), from *Schizosaccharomyces pombe* (PDB ID: 1TA9), from *Thermotoga maritima* (PDB ID: 1KQ3), from an unidentified organism (PDB ID: 5XN8), from *Citrobacter freundii* (CfGlyDH: Uniprot: P45511), from *Pseudomonas putida* (PpGlyDH: Uniprot: P50173), from *Enterobacter aerogenes* (Uniprot: A0A0H3FPM0_KLEAK), and 1JQ5), the glycerol 1-phosphate family from *Pyrobaculum calidifontis* (PDB ID: 5FB3), from *Methanocaldococcus jannaschii* DSM 2661 (PDB ID: 4RFL and 4RGQ), short-chain alcohol dehydrogenases from *Parageobacillus thermoglucosidasius* (PDB ID: 3ZDR) from *Fusobacterium nucleatum* subsp. (PDB ID: 6LIK), Iron-dependent 1,2-propanediol oxidoreductase from *Escherichia coli* (PDB ID: 2BI4) and lactaldehyde reductases from *Escherichia coli* (PDB ID: 1RRM), and medium-chain mannitol dehydrogenase from *Pseudomonas fluorescens* (PDB ID: 1LJ8). The position occupied by an aspartate highly conserved in GlyDH and archeal glycerol 1-phosphate dehydrogenases is highlighted with a blue box.

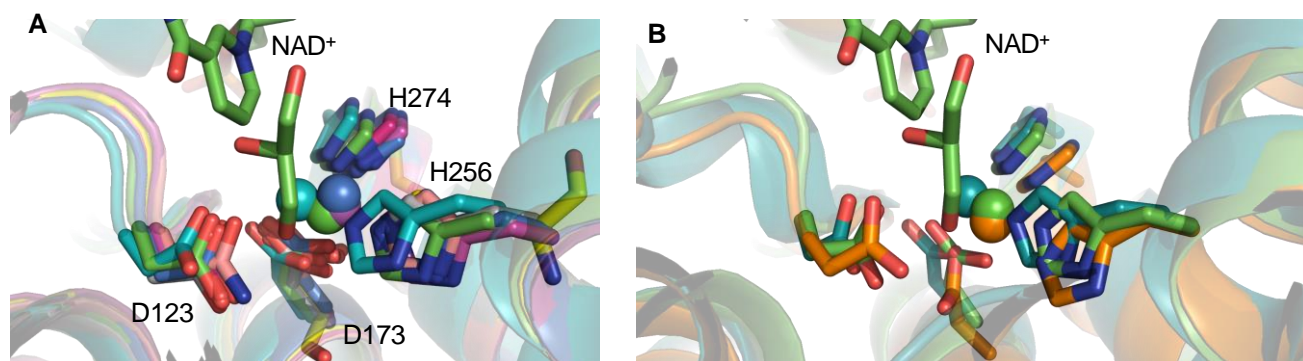


Figure S9. Structural alignment of BsGlyDH (PDB ID: 1JQ5, green) with GlyDHs (A) and archeal glycerol 1-phosphate dehydrogenase (B). The selected GlyDH are from *Escherichia coli* K-12 (PDB ID: 5ZXL, violet), from *Serratia plymuthica* A30 (PDB ID: 4MCA, yellow), from *Bacillus coagulans* (PDB ID: 6CSJ, light pink), from *Thermotoga maritima* (PDB ID: 1KQ3, blue), from an unidentified organism (PDB ID: 5XN8, pink) and from *Sinorhizobium meliloti* (PDB ID: 3UHJ, turquoise). The selected archeal glycerol 1-phosphate dehydrogenases are from *Pyrobaculum calidifontis* (PDB ID: 5FB3, orange), from *Methanocaldococcus jannaschii* DSM 2661 (PDB ID: 4RFL, cyan). The marked residues are the catalytic triad that coordinates the Zn^{2+} atom and the conserved Asp residue that act as base for the polarization of the C2 hydroxyl group. The numbers refer to the position in BsGlyDH (PDB ID: 1JQ5, green)

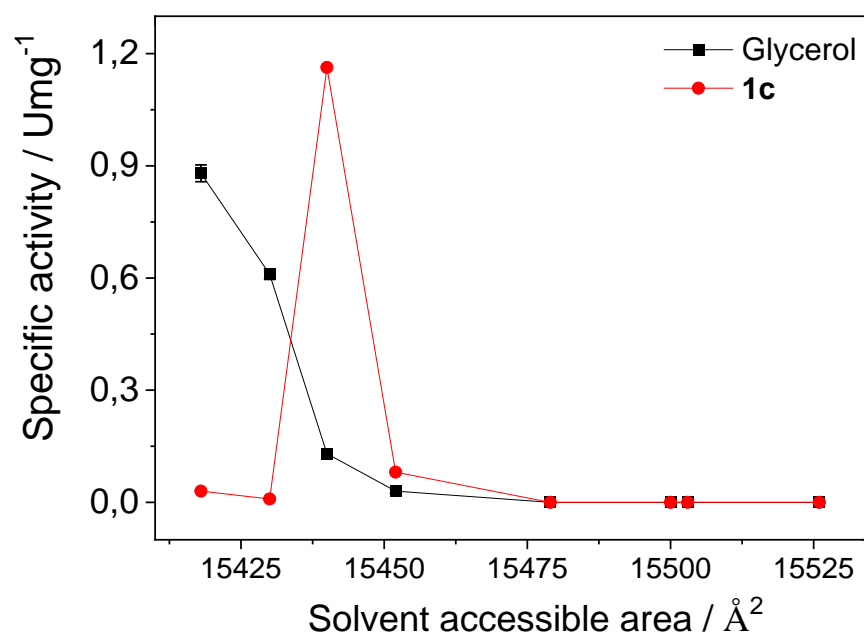


Figure S10. Effect of the solvent accessible area in the activity of BsGlyDH variants. All reactions were carried out at 100 mM of substrate, 1 mM NAD⁺ in sodium phosphate buffer 100 mM pH 7 at 30 °C.

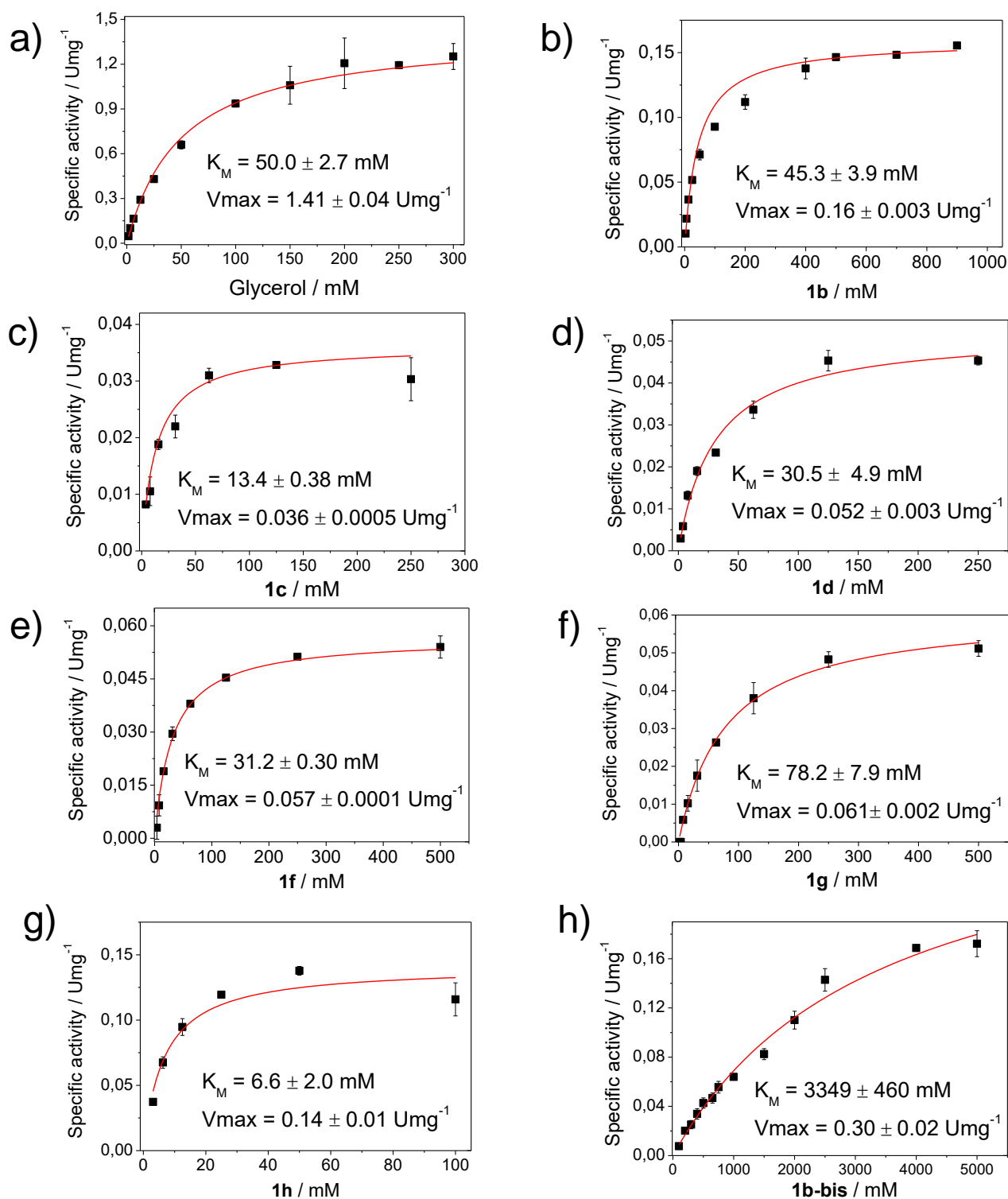


Figure S11. Kinetic parameters of BsGlyDH-WT. In all cases, 1 mM NAD⁺ in 100 mM sodium phosphate buffer pH 7 at 30 °C.

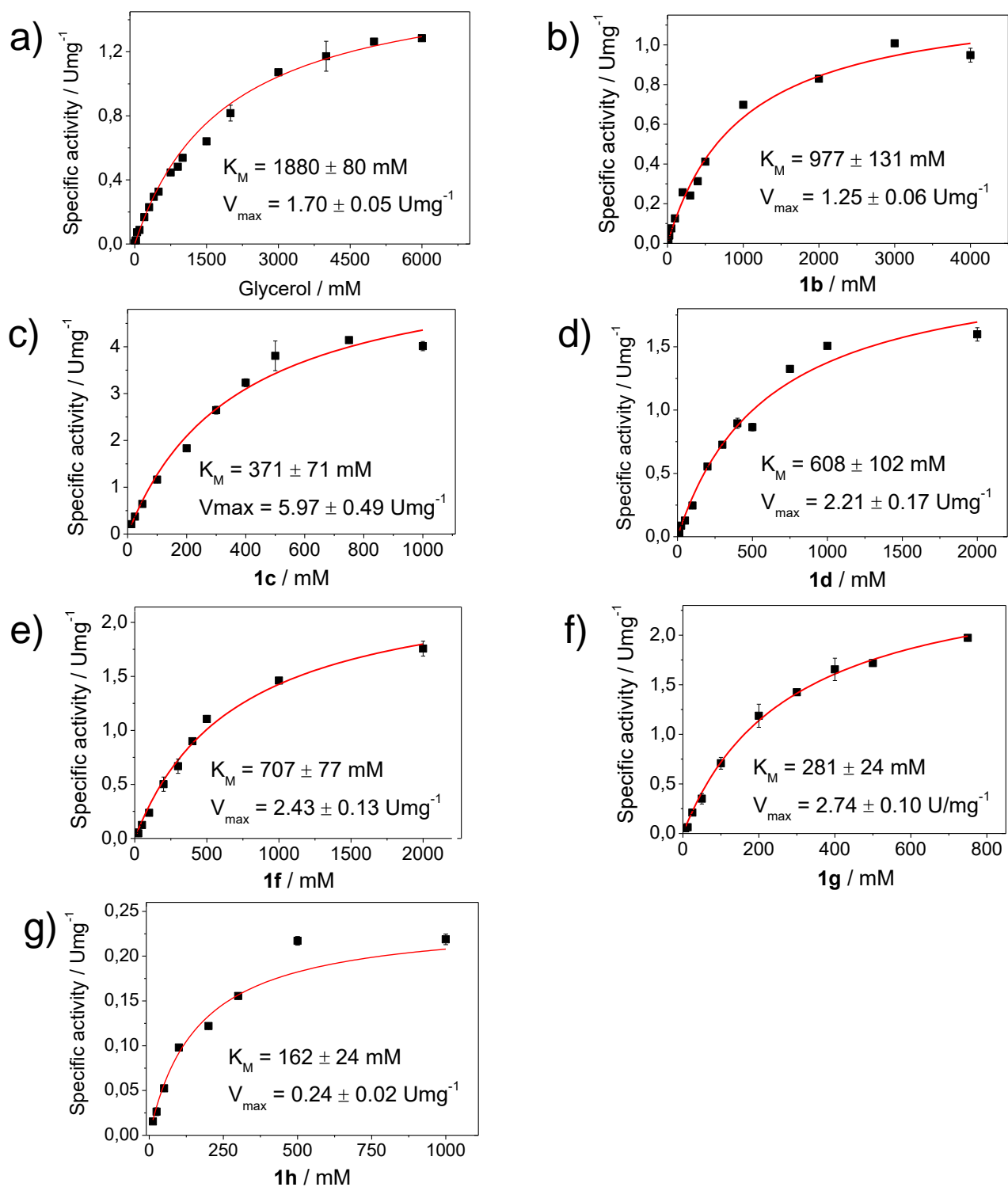


Figure S12. Kinetic parameters of BsGlyDH-L252A. In all cases, 1 mM NAD⁺ in 100 mM sodium phosphate buffer pH 7 at 30 °C.

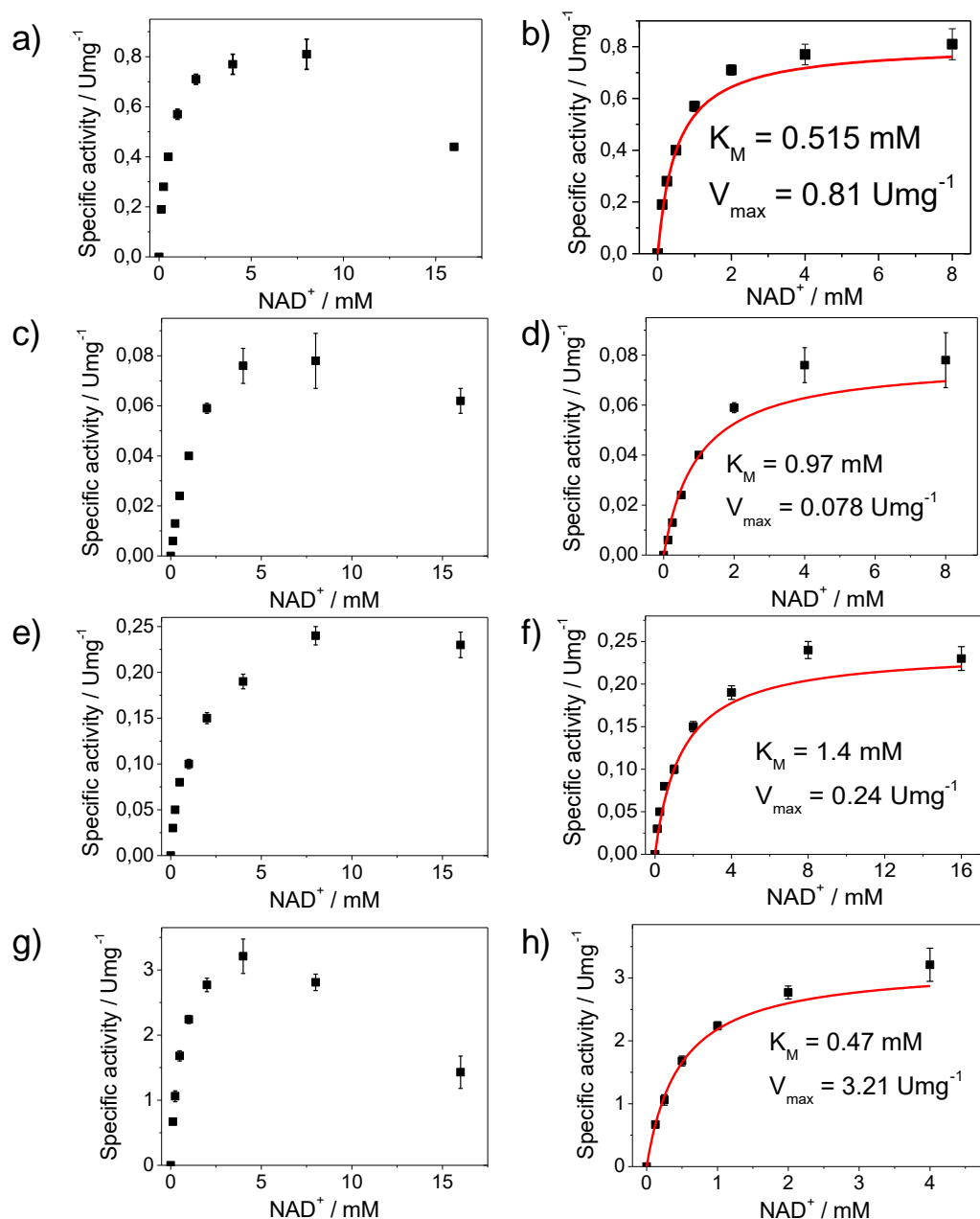


Figure S13. Kinetic parameters of BsGlyDH variants with NAD⁺. BsGlyDH-WT: Reaction mixture 100 mM glycerol in 100 mM in sodium phosphate buffer pH 7 at 30 °C (a). Michaelis-Menten data fitting without considering the NAD⁺ inhibition at concentration higher than 8 mM. Kinetic parameters of BsGlyDH-L252A (b). Reaction mixture 100 mM glycerol in 100 mM in sodium phosphate buffer pH 7 at 30 °C (c). Michaelis-Menten data fitting without considering the NAD⁺ inhibition at concentration higher than 8 mM (d). Reaction mixture 100 mM **1c** in 100 mM in sodium phosphate buffer pH 7 at 30 °C (e). Michaelis-Menten data fitting (no inhibition). G) Reaction mixture 100 mM **1c** in 100 mM in sodium phosphate buffer pH 9 at 30 °C (f). Michaelis-Menten data fitting without considering the NAD⁺ inhibition at concentration higher than 4 mM (h).

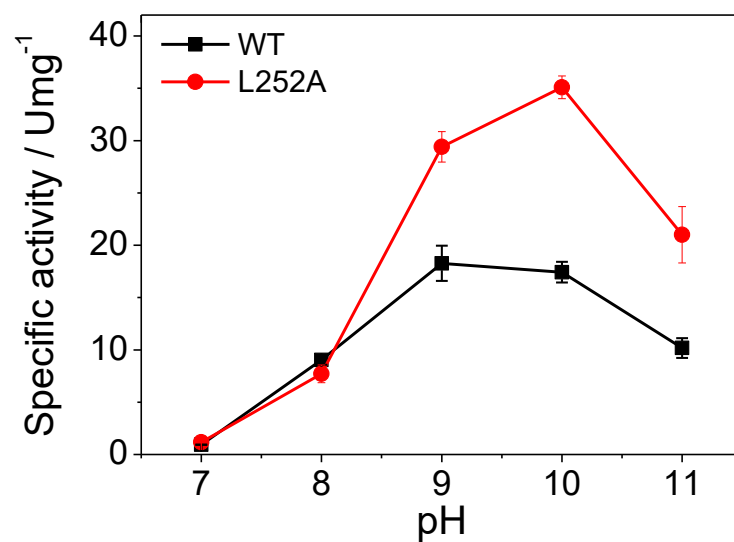


Figure S14. pH profile of GlyDH WT and mutant L252A using 100 mM of glycerol (black squares) and **1c** (red circles), 1 mM NAD⁺ in 100 mM buffer at 30 °C.

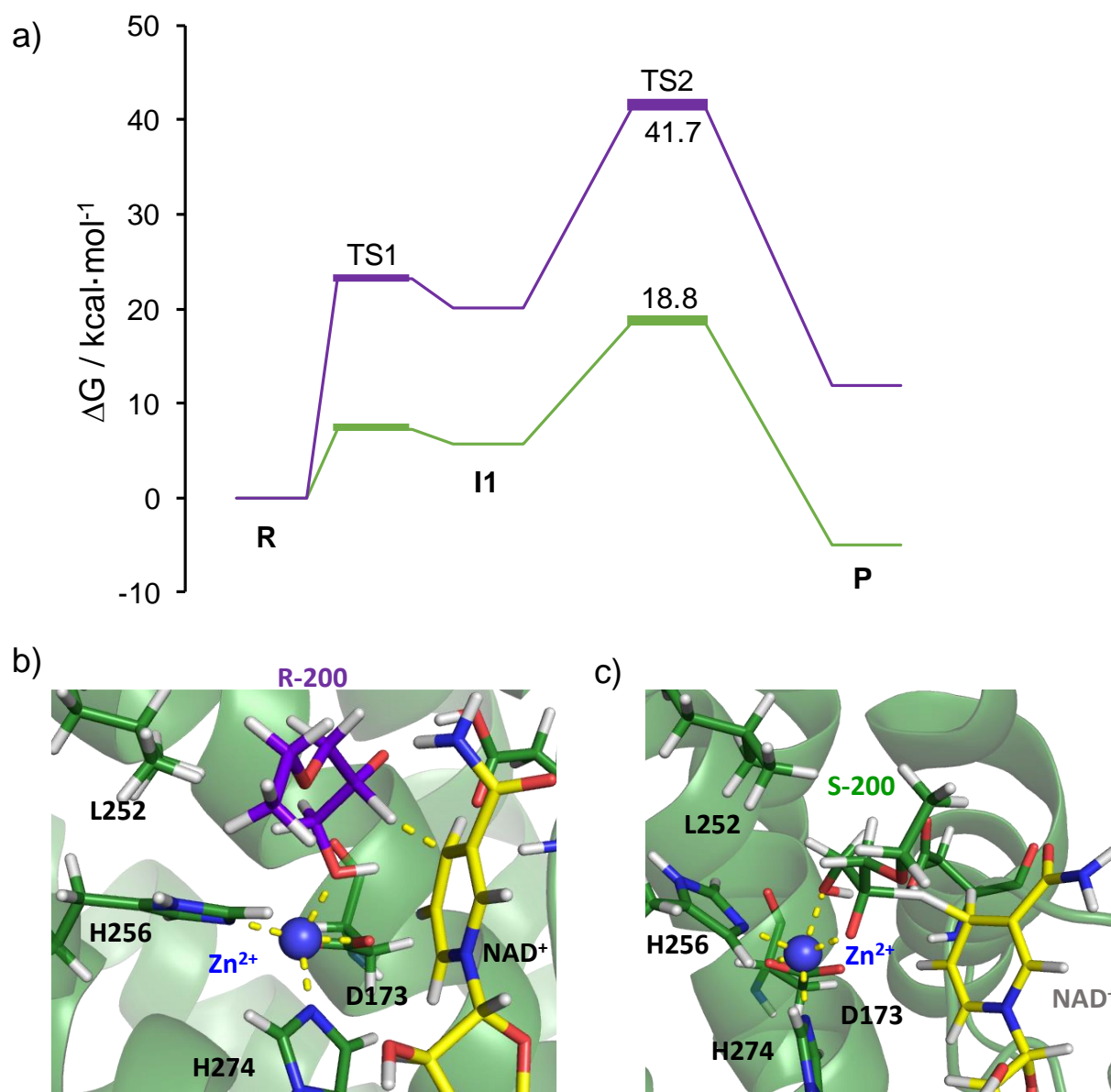


Figure S15. M06-2X/6-31+G(d,p):PM3/MM PMFs with ZPE corrections for mechanism 2 of the wild-type BsGlyDH system with *R*-**1c** enantiomer (in purple) and *S*-**1c** enantiomer (in green). R: *R*-**1c** / TS1: Transition state 1 / I1:alkoxide intermediate / TS2: Transition state 2 / P: 3-ethoxy-1-hydroxyacetones (a). Localised transition state structures of the second step for the b) *R*-**1c** enantiomer (purple) and (b) *S*-**1c** enantiomer (green) (c).

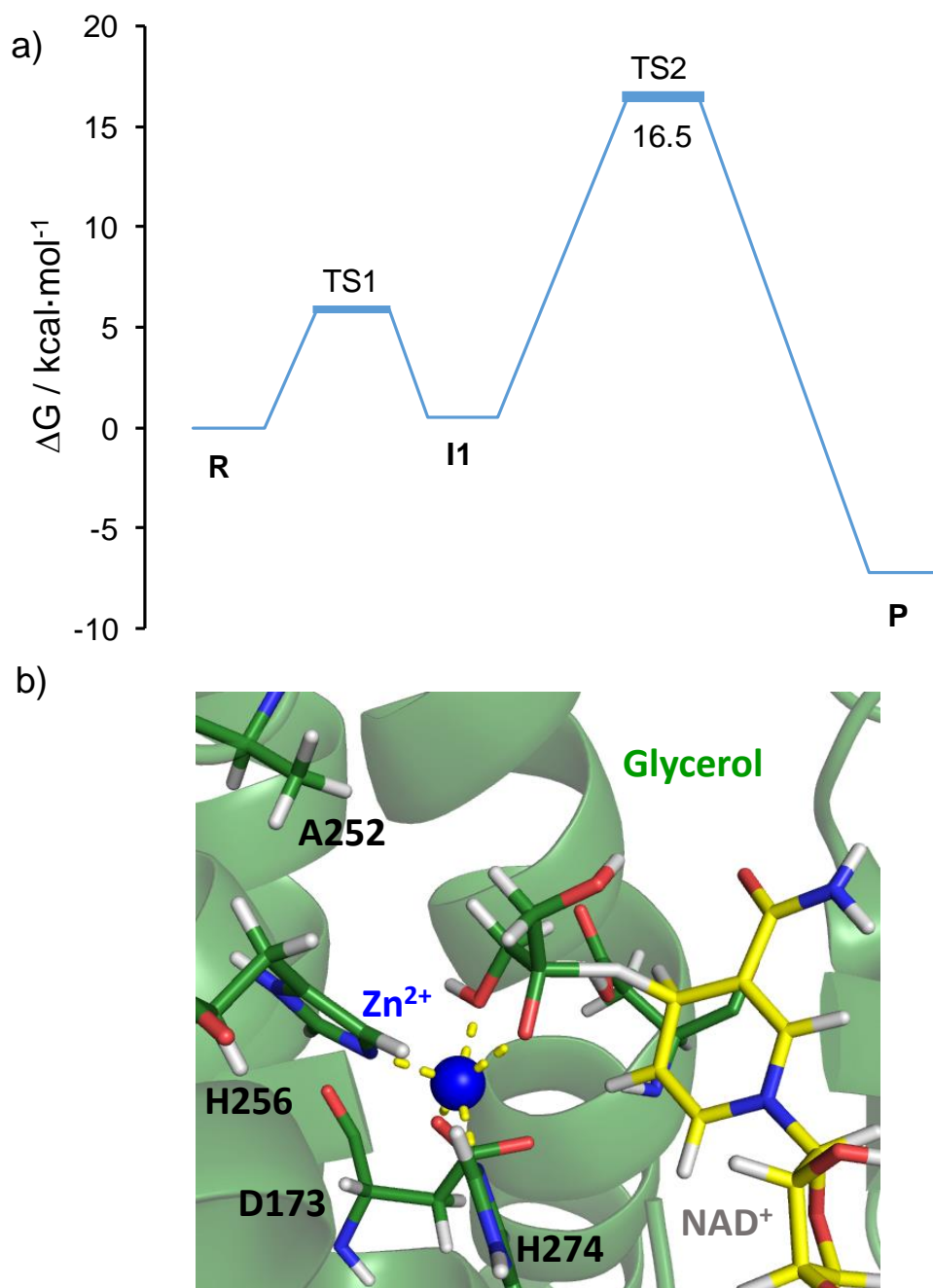


Figure S16. M06-2X/6-31+G(d,p):PM3/MM PMFs with ZPE corrections for mechanism 2 of the BsGlyDH-L252A system with glycerol. R: glycerol / TS1: Transition state 1 / I1:alkoxide intermediate / TS2: Transition state 2 / P: Dihydroxyacetone (a) and localised transition state structure of the second step (b).

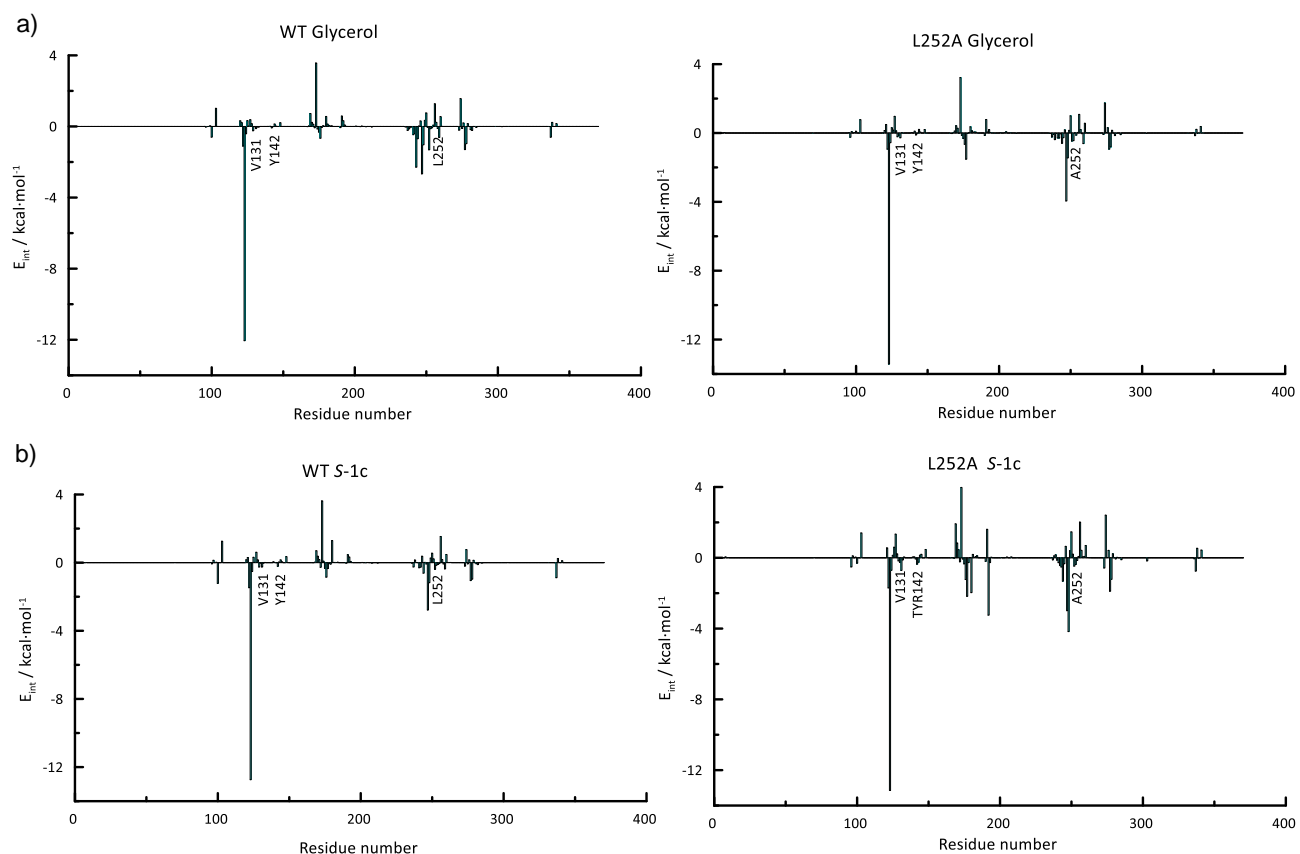


Figure S17. Average interaction energies (electrostatic plus Lennard-Jones) by residue between the enzyme and the substrates over 1000 structures of the QM/MM MD simulations on the reactant state; a) WT and L252A mutant with glycerol as substrate, b) WT and L252A mutant with S-1c as substrate. The energies are in $\text{kcal}\cdot\text{mol}^{-1}$.

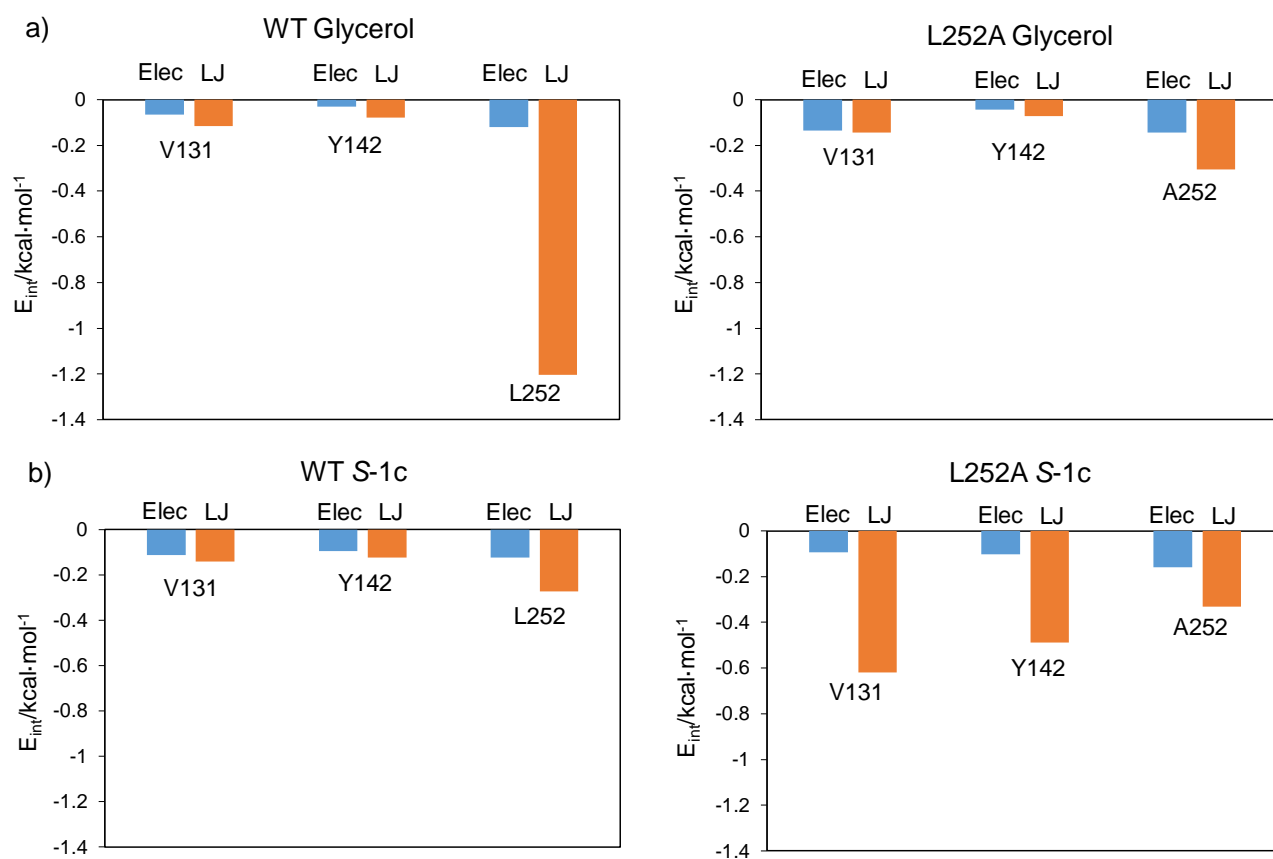


Figure S18. Average electrostatic (Elec) and Lennard-Jones (LJ) contributions to the interaction energy between the key residues and the substrates over 1000 structures of the QM/MM MD simulations on the reactant state; a) WT and L252A mutant with glycerol as substrate, b) WT and L252A mutant with S-1c as substrate. The energies are in kcal·mol⁻¹.

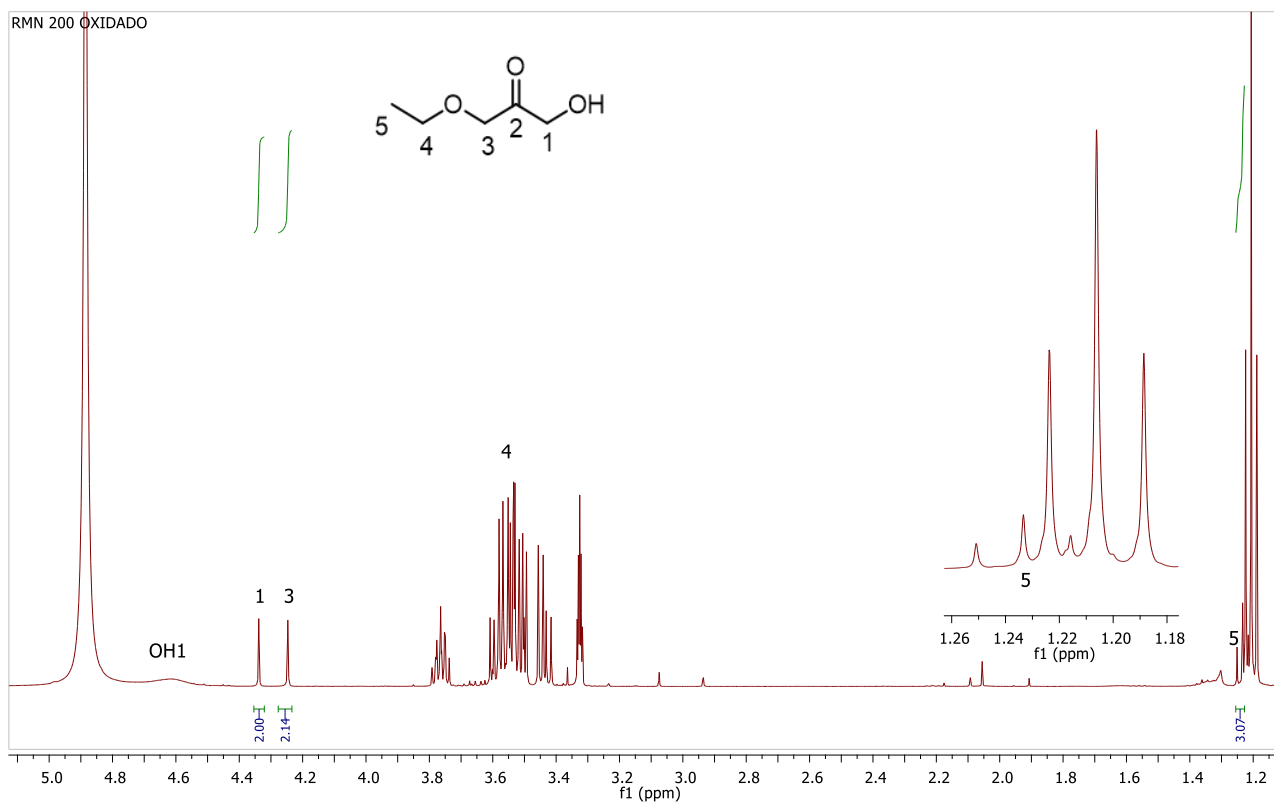


Figure S19. ^1H NMR of the reaction mixture of the oxidation of **1c**. The assigned signals correspond to the oxidised product of **1c**, 3-phenoxy-1-hydroxypropan-2-one.

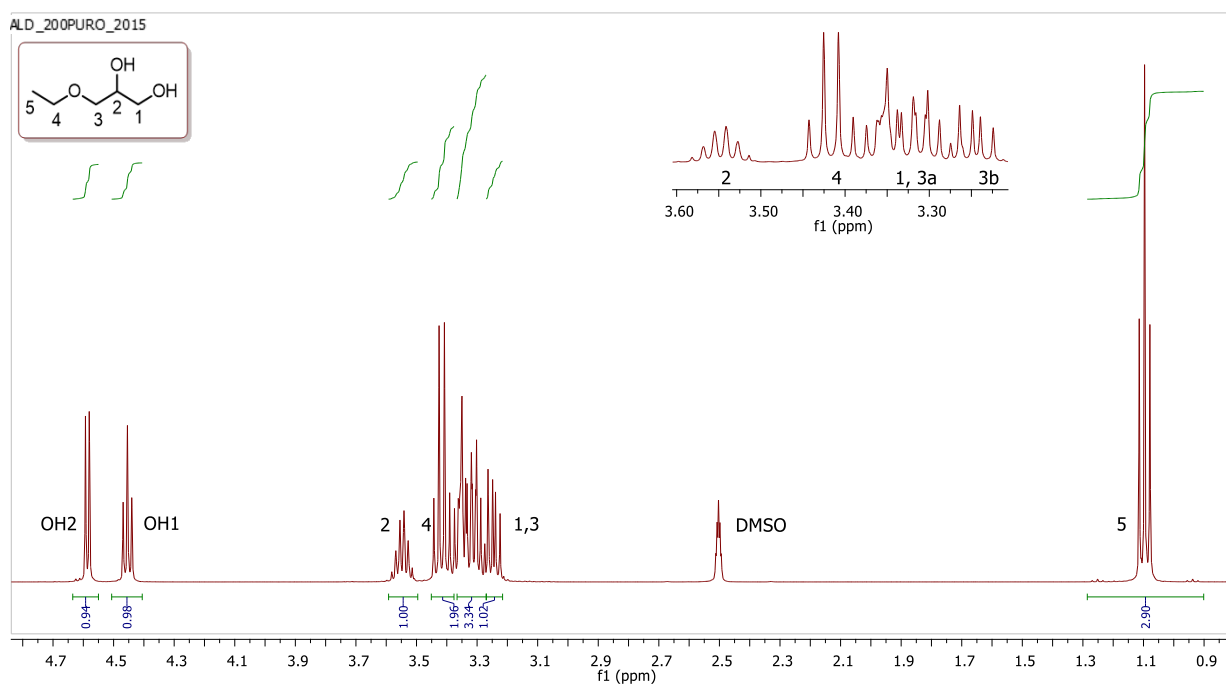


Figure S20. ^1H NMR of the pure glyceryl monoether **1c**.

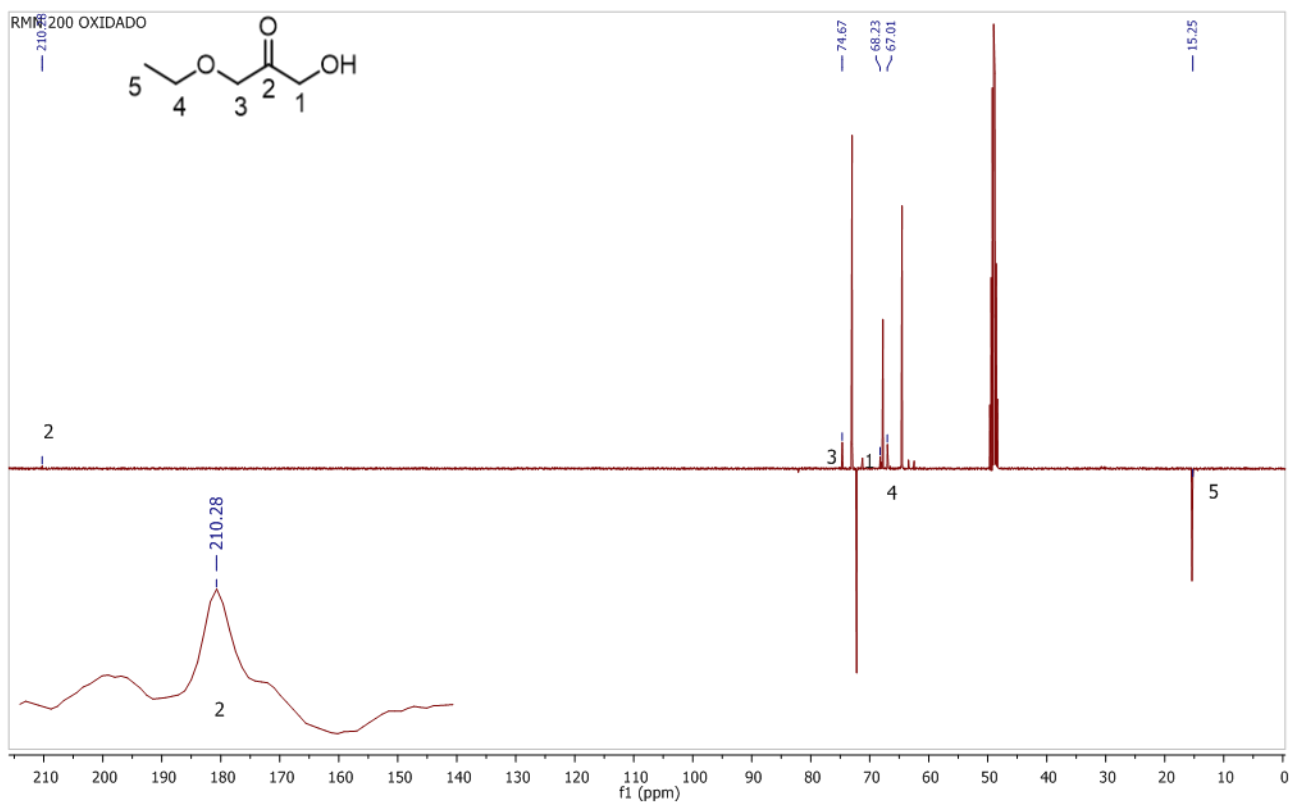


Figure S21. ^{13}C NMR (APT) of the reaction mixture of the oxidation of **1c**. The assigned signals correspond to the oxidised product of **1c**; 3-phenoxy-1-hydroxypropan-2-one.

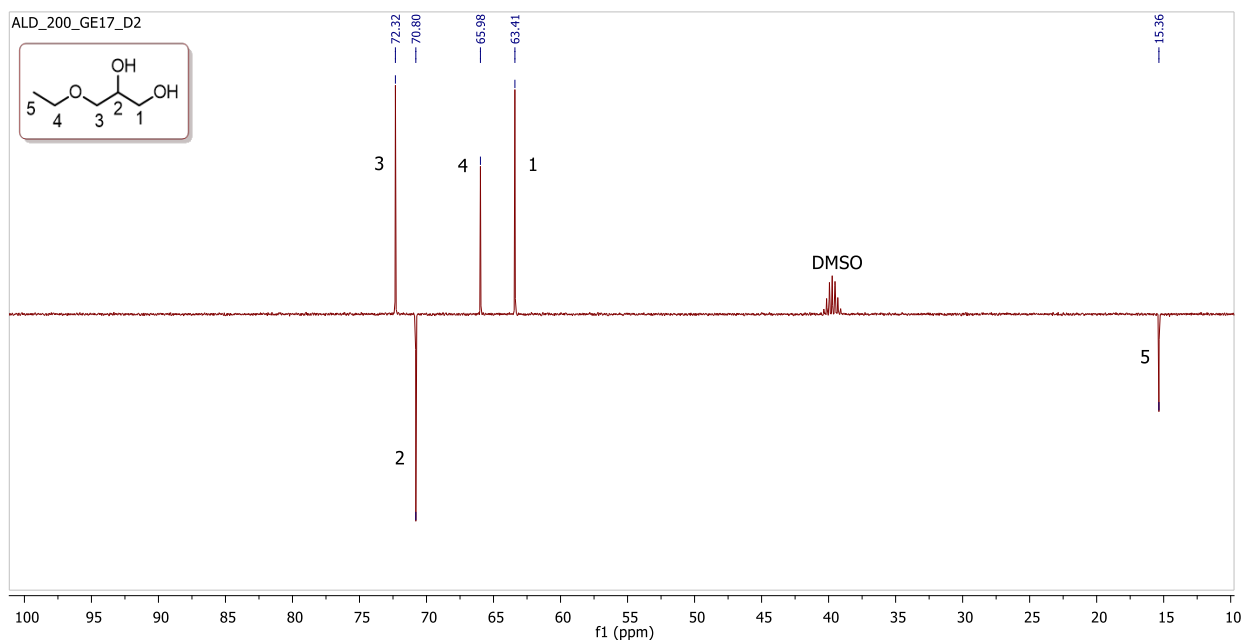
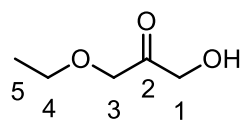
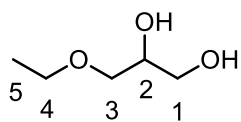


Figure S22. ^{13}C NMR (APT) of the pure glyceryl monoether **1c**.



3-Ethoxy-1-hydroxyacetone, C₅O₃H₁₀.

¹H NMR (400 MHz, [d₆]MeOH, 25 °C): δ 4.50-4.68 (m, 1H, OH₁), 4.32 (s, 2H, H₁), 4.23 (s, 2H, H₃), ~3.50 (q, 2H, H₄), 1.23 (t, 3H, *J* = 7.0 Hz, H₅). **¹³C NMR** (100 MHz, [d₆]MeOH, 25 °C): δ 210.3 (C=O, C₂), 74.7 (CH₂, C₃), 68.2 (CH₂, C₁), 67.0 (CH₂, C₄), 15.3 (CH₃, C₅).



3-Ethoxypropan-1,2-diol (1c), C₅O₃H₁₂. Colorless liquid.

¹H NMR (400 MHz, [d₆]DMSO, 25 °C): δ 4.59 (d, 1H, *J* = 5.1 Hz, OH₂), 4.45 (t, 1H, *J* = 5.7 Hz, OH₁), 3.55 (sext, 1H, *J* = 5.3 Hz, H₂), 3.42 (q, 2H, *J* = 7.0 Hz, H₄), 3.27-3.37 (m, 3H, H₁, H_{3a}), 3.24 (dd, 1H, *J*_{gem} = 9.9 Hz, *J* = 6.1 Hz, H_{3b}), 1.10 (t, 3H, *J* = 7.0 Hz, H₅). **¹³C NMR** (100 MHz, [d₆] DMSO, 25 °C): δ 72.3 (CH₂, C₃), 70.8 (CH, C₂), 66.0 (CH₂, C₄), 63.4 (CH₂, C₁), 15.4 (CH₃, C₅).

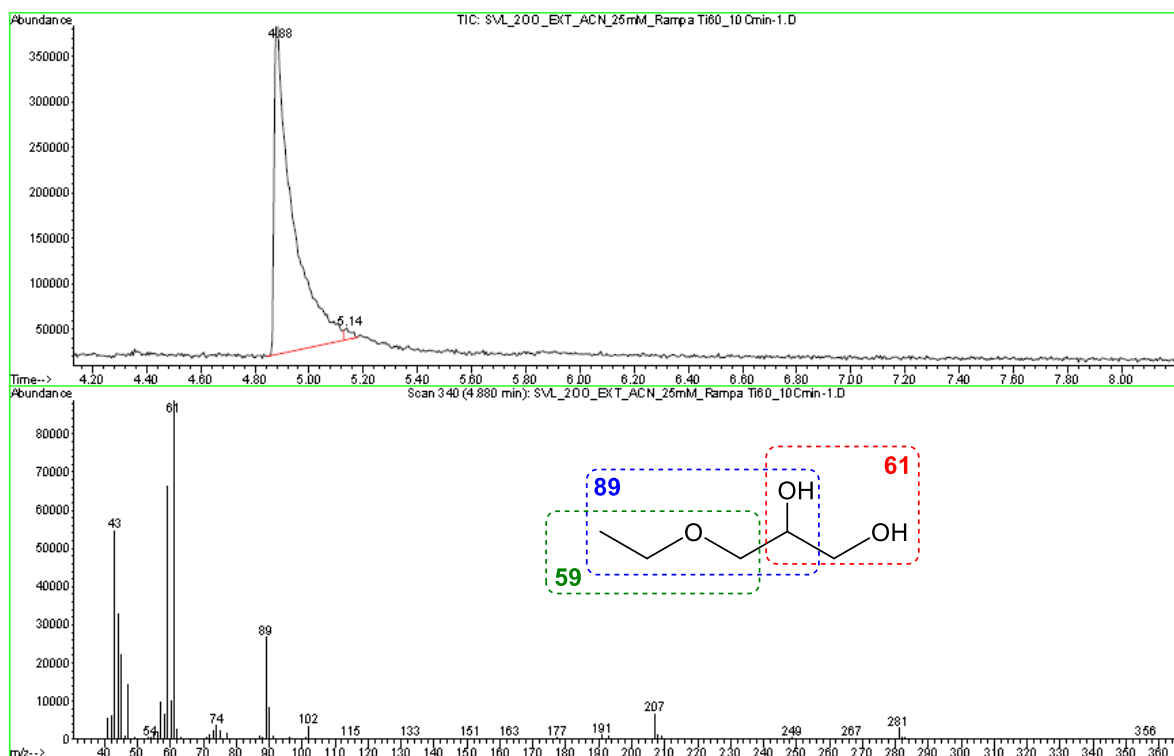


Figure S23. GC-MS analysis of sample: Negative reaction control (without enzyme), **1c**, retention time 4.88 min.

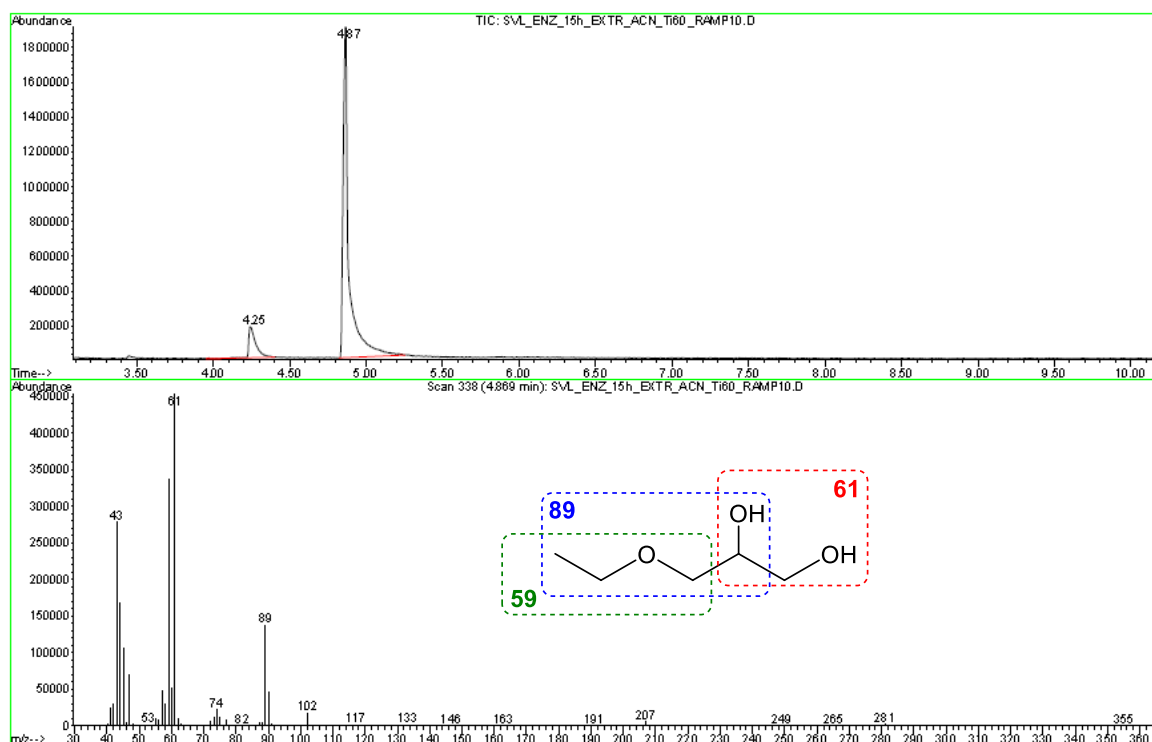


Figure S24. GC-MS analysis. Sample: Enzymatic reaction, remnant substrate **1c**, retention time 4.87 min.

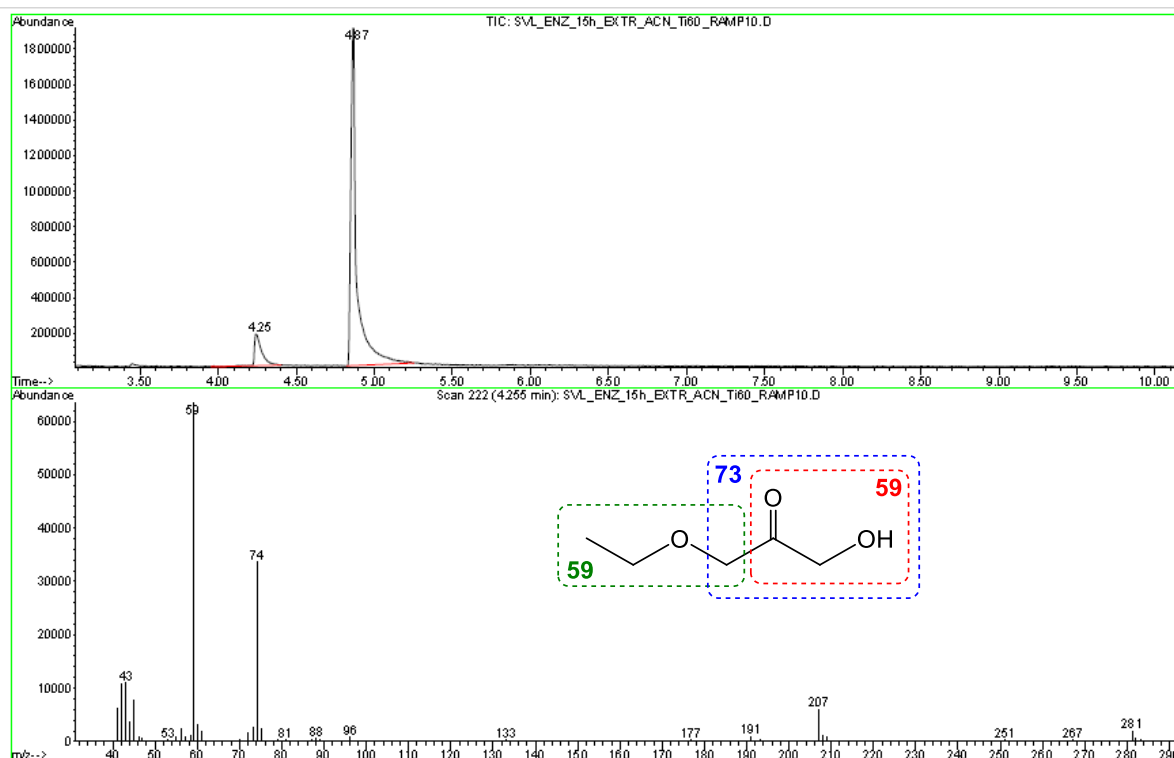


Figure S25. GC-MS analysis. Sample: Enzymatic reaction: oxidised product of **1c**, **3-ethoxy-1-hydroxyacetone** retention time 4.25 min.

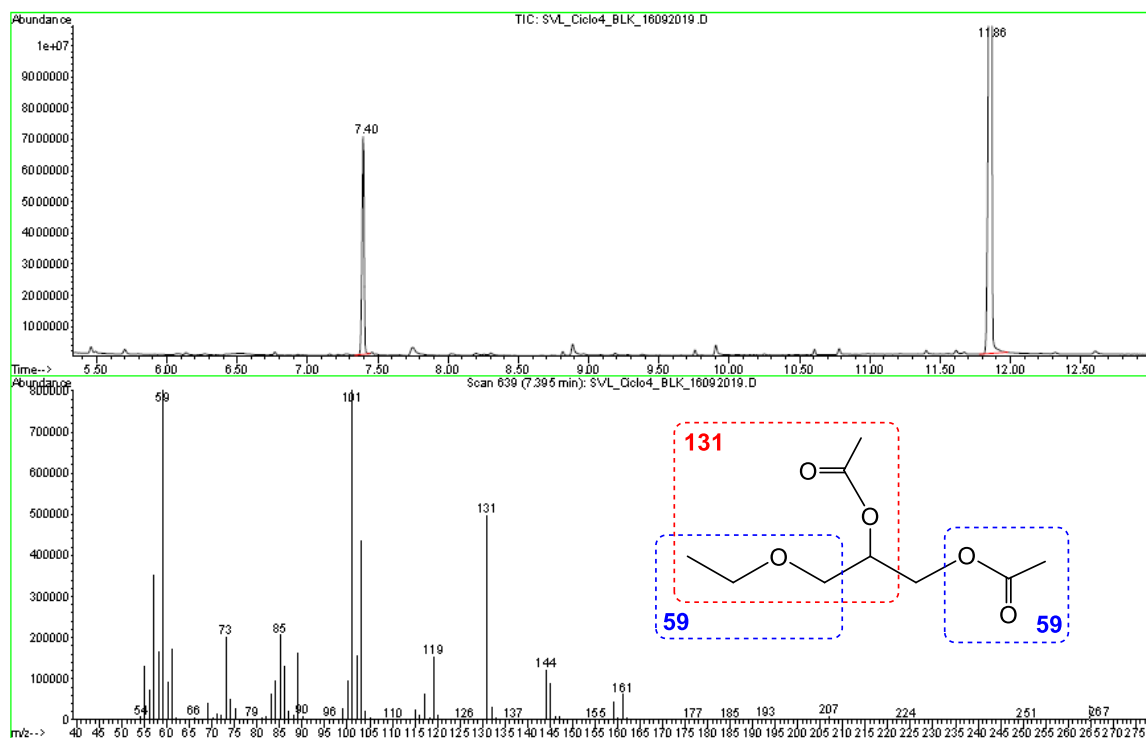


Figure S26. GC-MS analysis. Sample: Negative reaction control (without enzyme): acetylated substrate, retention time 7.39 min.

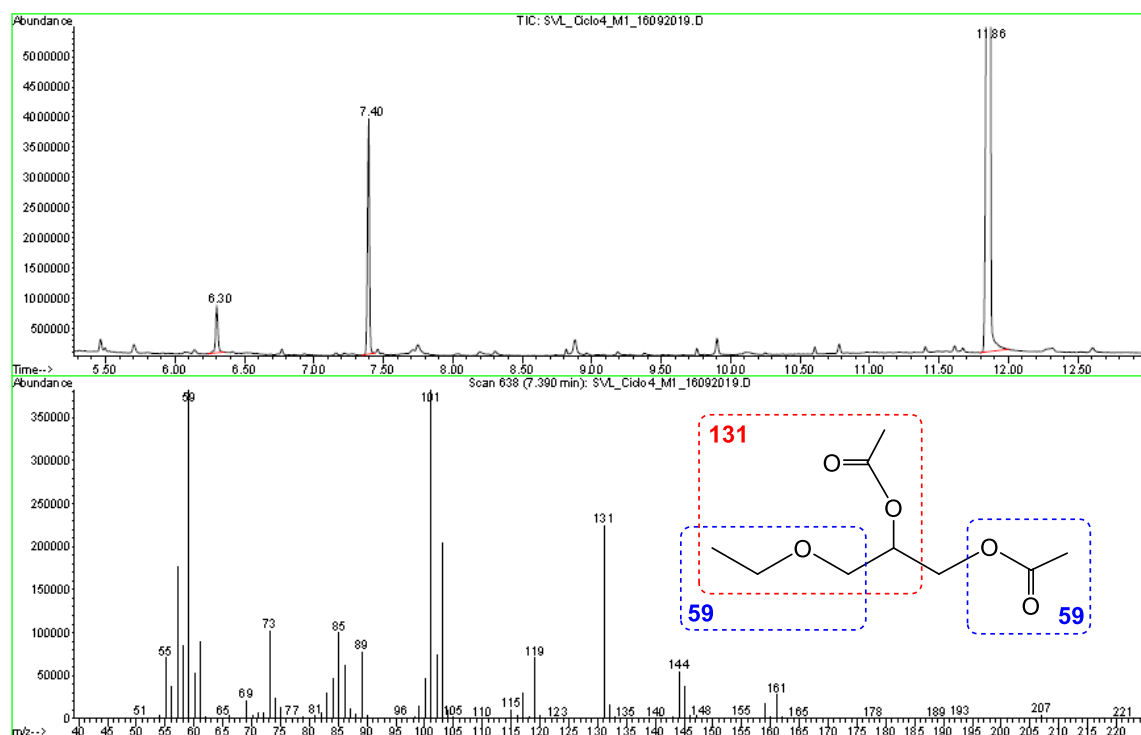


Figure S27. GC-MS analysis. Sample: Enzymatic reaction: acetylated substrate 1c, retention time 7.39 min.

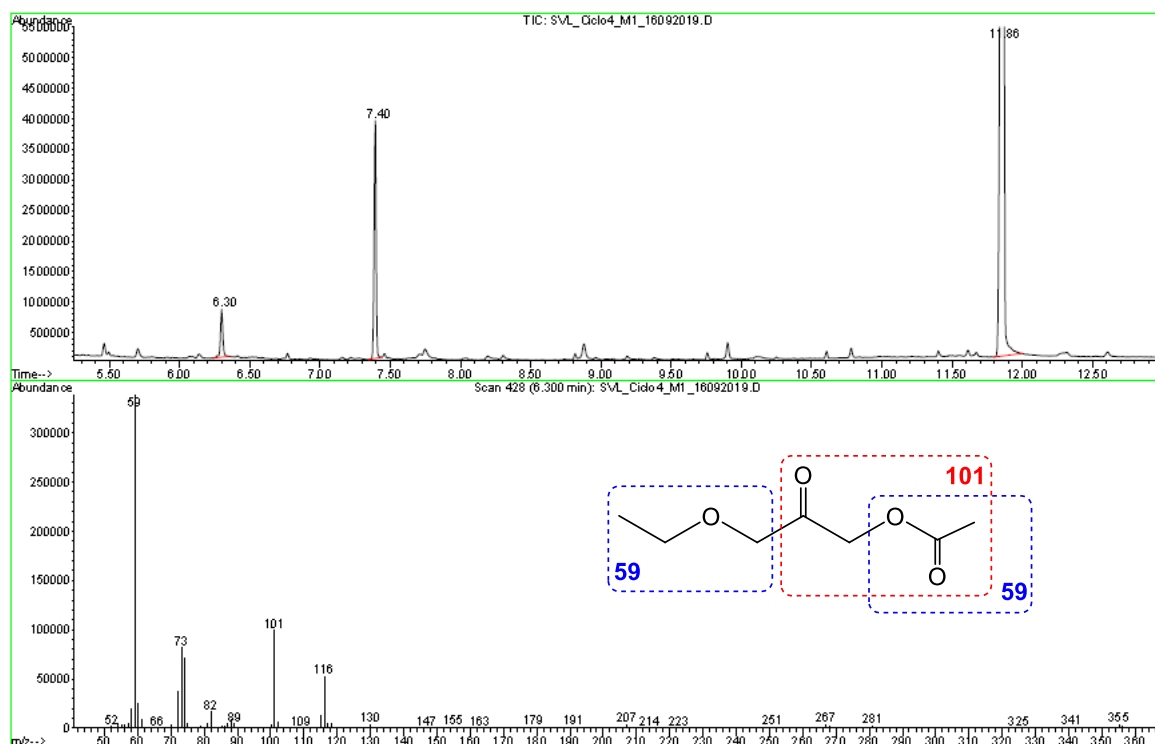


Figure S28. GC-MS analysis. Sample: Enzymatic reaction: acetylated 3-phenoxy-1-hydroxypropan-2-one , retention time 6.30 min.

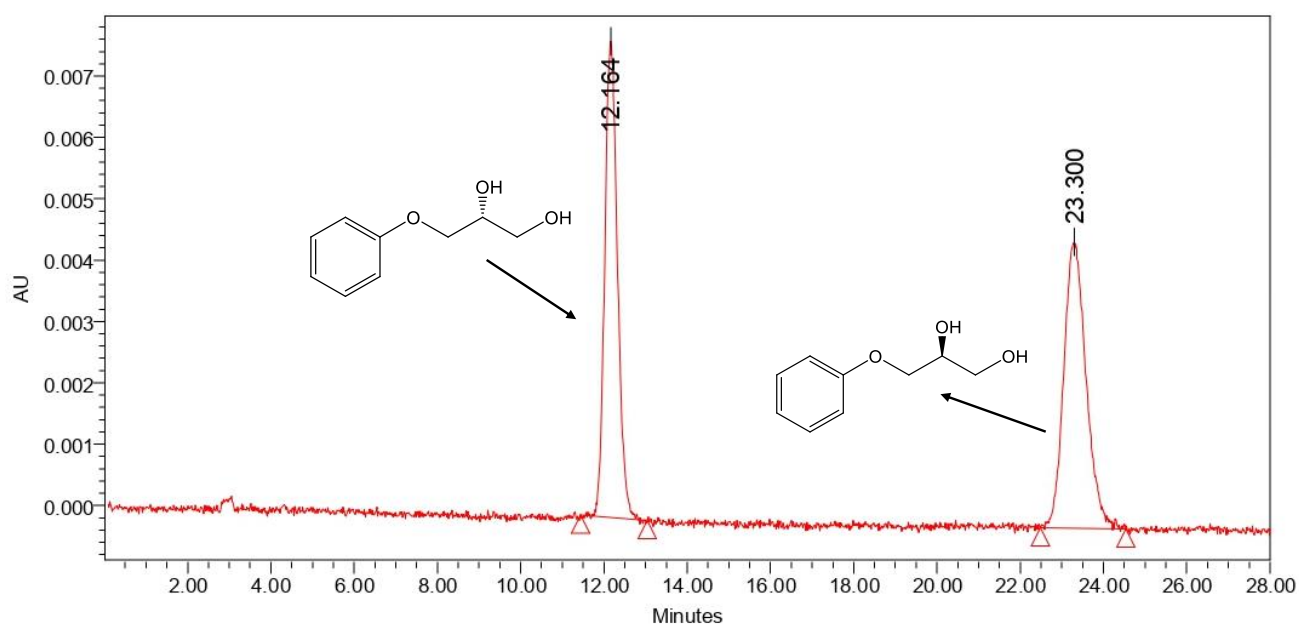


Figure S29. Chiral HPLC chromatogram of standard *rac*-1h.

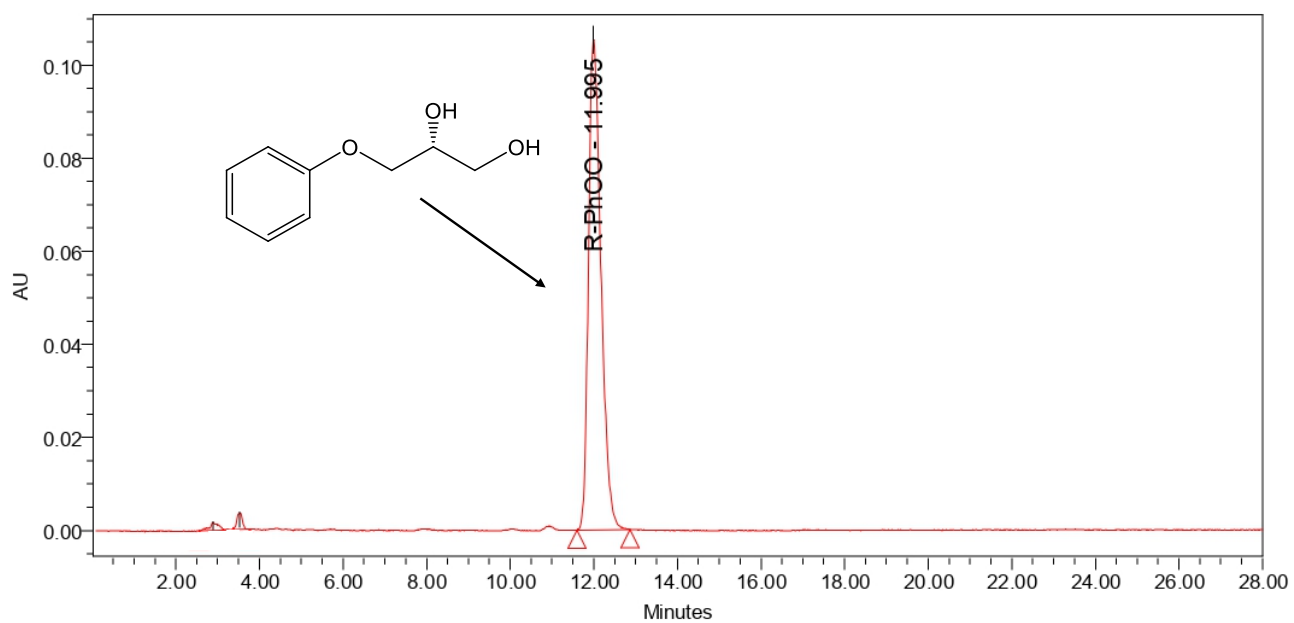


Figure S30. Chiral HPLC chromatogram of standard *R*-1h.

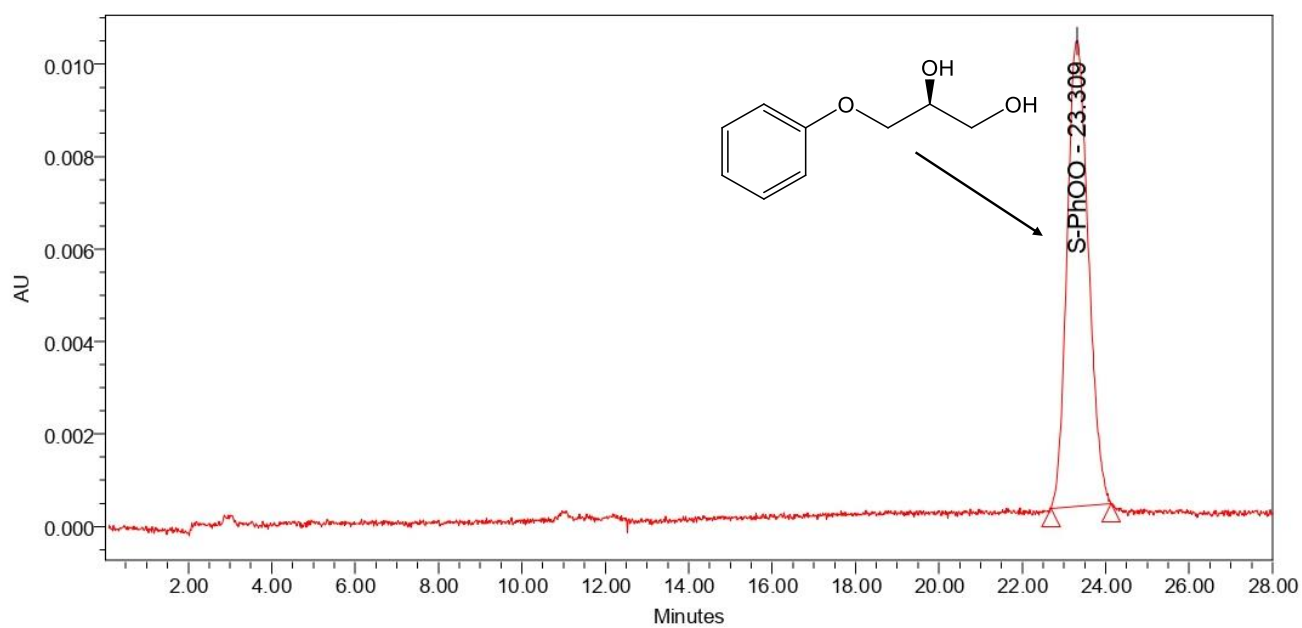


Figure S31. Chiral HPLC chromatogram of standard *S*-1h.

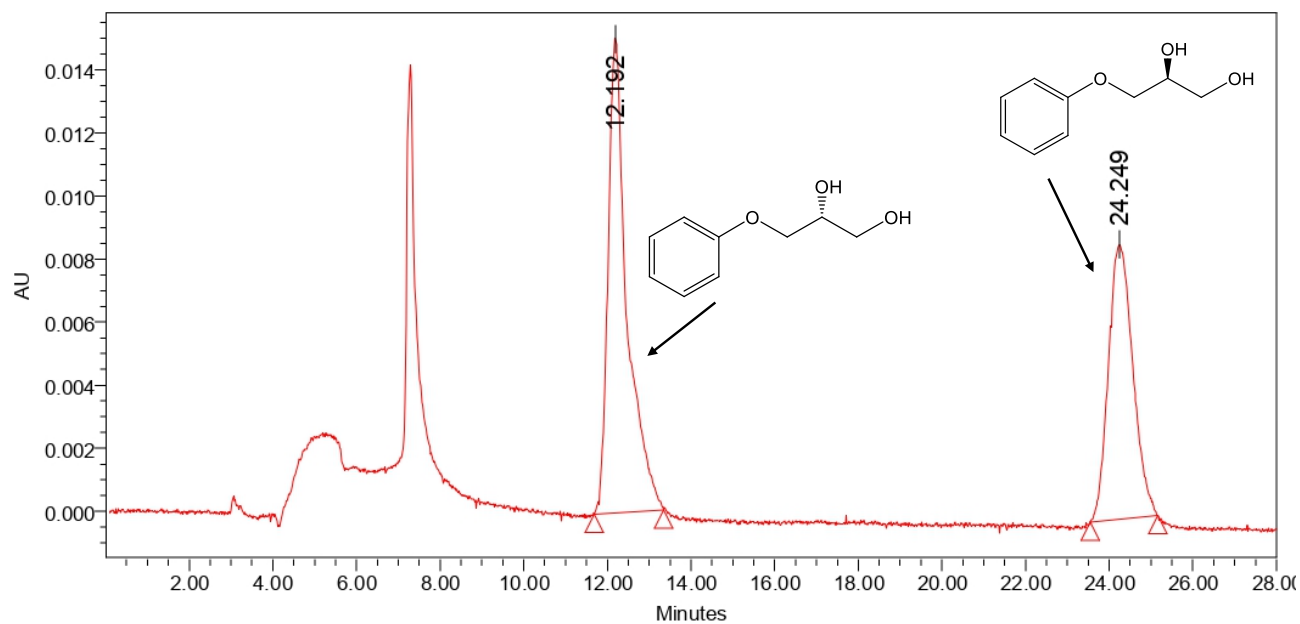


Figure S32. Chiral HPLC chromatograms of negative reaction control mixture at 72 h.

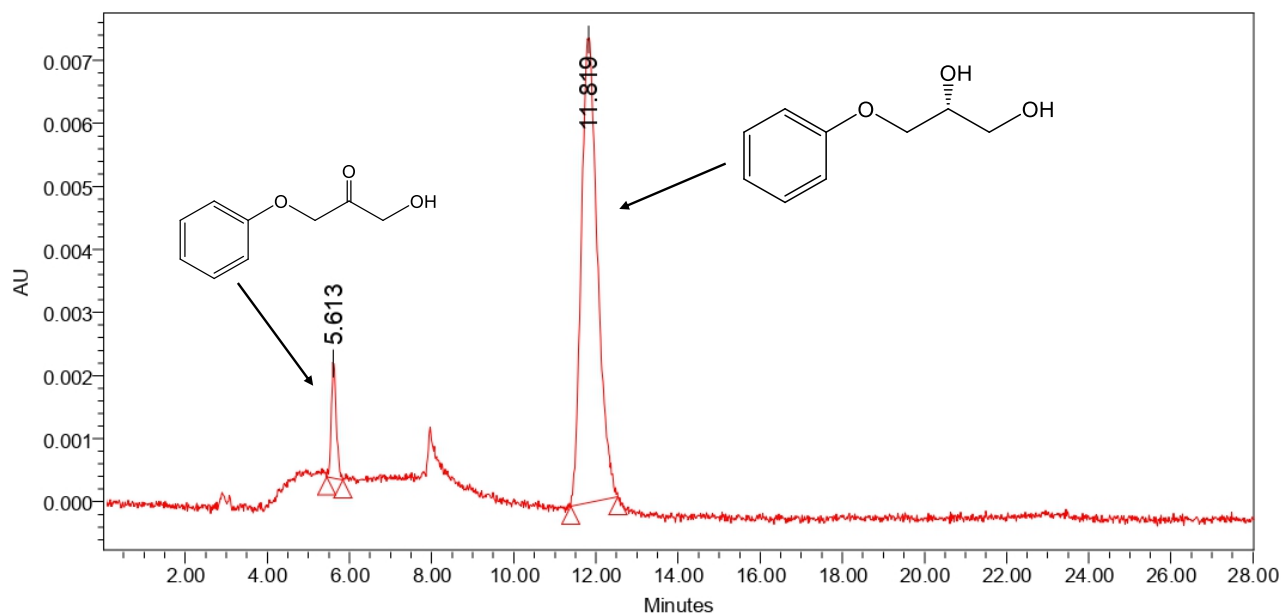


Figure S33. Chiral HPLC chromatograms of enzymatic reaction samples of *rac*-**1h** at 72 h.

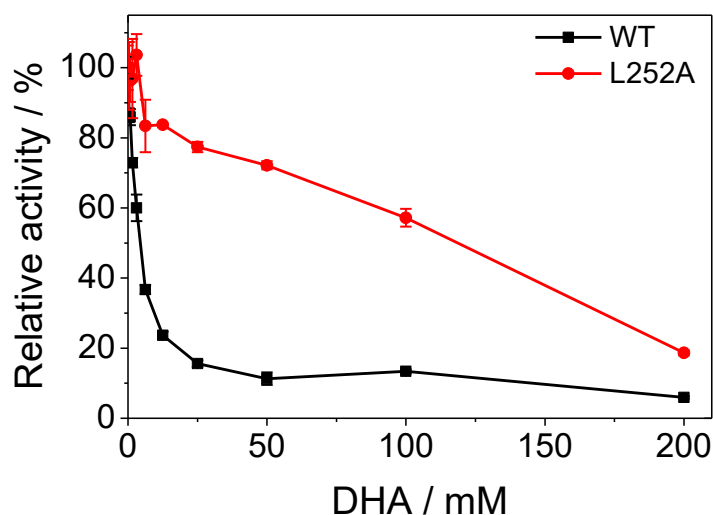


Figure S34. Inhibition of BsGlyDH enzymes by DHA. Reaction conditions consisted in 100 mM of glycerol or *rac-1c*, 1 mM NAD⁺ in 100 mM sodium phosphate buffer pH 7 or bicarbonate buffer pH 9, respectively, at 30 °C.

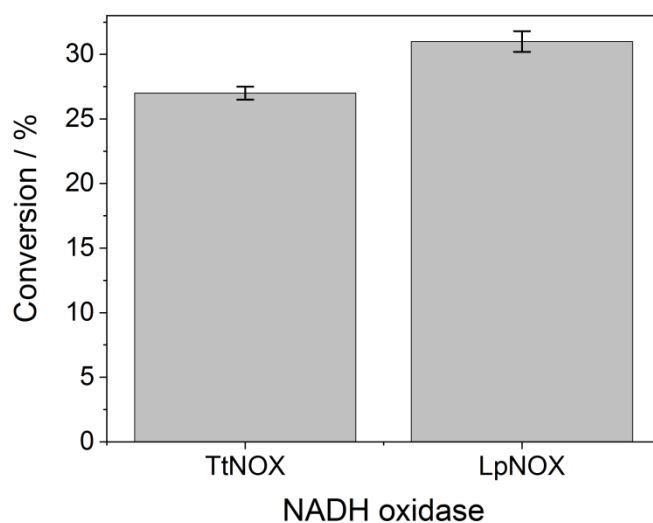


Figure S35. Oxidation of **1c** catalyzed by immobilised GlyDH-L252-AG-Co²⁺ and different immobilised NADH oxidases. In the case of LpNOX, this enzyme was co-immobilized with GlyDH-L252A con Ag-Co²⁺ (100 mg). In the case of TtNOX, this enzyme was co-immobilized with HICAT on AG-GX (120 mg) and mixed with GlyDH-L252A-AG-Co²⁺ (100 mg). Reaction mixture consisted in 300 μ L of 25 mM of *rac-1c*, 1 mM NAD⁺, 150 μ M FAD⁺ in 100 mM sodium phosphate buffer at pH 7 at 30 °C after 24 hours.

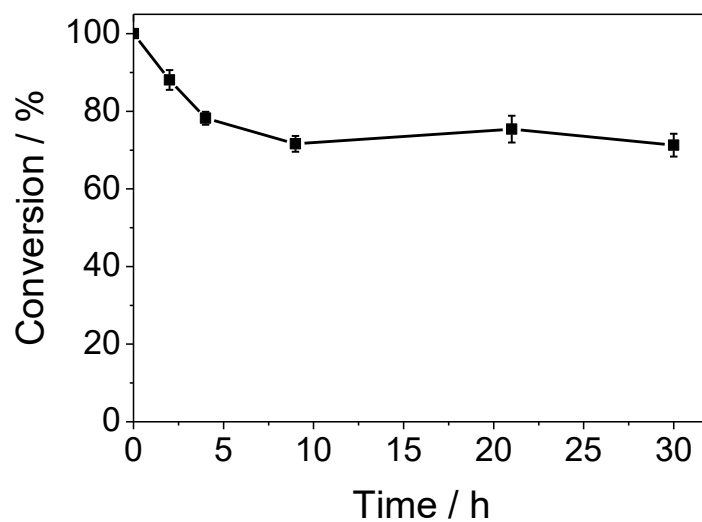


Figure S36. Batch reactor. Heterogeneous biocatalyst BsGlyDH-L252A co-immobilised with Lp-NOX on AG- Co^{2+} (5 g biocatalyst). Reaction mixture consisted in 50 mL of 20 mM of *rac*-**1c**, 1 mM NAD^+ , 150 μM FAD^+ in 100 mM sodium phosphate buffer at pH 7 at 30 °C.

3. Supplementary tables

Table S1. Glyceryl ethers employed as substrates in this work.

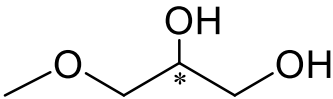
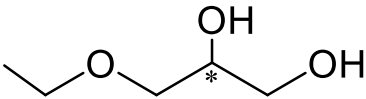
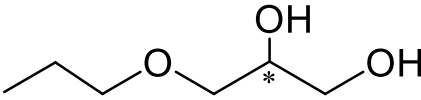
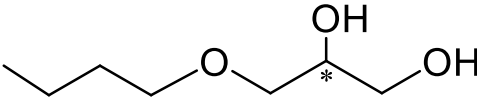
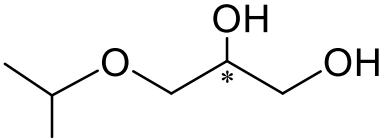
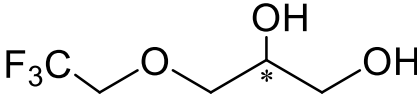
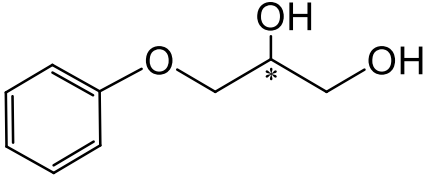
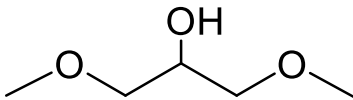
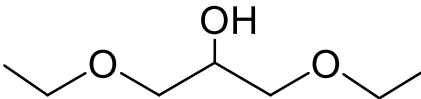
Substrate	Structure	Abbreviation
3-methoxypropan-1,2-diol		1b
3-ethoxypropan-1,2-diol		1c
3-propoxypropan-1,2-diol		1d
3-butoxypropan-1,2-diol		1e
3-isopropoxypropan-1,2-diol		1f
3-(2,2,2-trifluoroethoxy)propan-1,2-diol		1g
3-phenoxypropan-1,2-diol		1h
1,3-dimethoxypropan-2-ol		1b-bis
1,3-diethoxypropan-2-ol		1c-bis

Table S2. Design of mutated positions in the BsGlyDH primary sequence.

Name	Mutation position	Native residue	Substituted residue	Primer (5'-3')
V131A-F	131	V	A	gtgctctttctgcgatataattctgatg
V131A-R	131	V	A	catcagaatatatcgcagaaagagcac
Y142A-F	142	Y	A	cgtatttgaaagcgcgcgttttataaaaagaatcc
Y142A-R	142	Y	A	tttataaaaacgcgcgctttcaaatacg
L252A-F	252	L	A	gaaagcggcggtgcggcagcggctcatg
L252A-R	252	L	A	catgagccgctgccgcaccgccgctttcaaaacc
D123N-F	123	D	N	ctgcttcaactaatgcgccaactagt
D123N-R	123	D	N	ctagttggcgcattagttgaagcagctg

Table S3. Activity of different glycerol dehydrogenases towards glycerol ethers.

Substrate	<i>Cellulomonas</i> sp (U/mg) ^a	<i>Bacillus stearothermophilus</i> (U/mg) ^a
Glycerol (1a)	4.674 (100)	0.879 (1.0)
1b	0.325 (7.0)	0.091 (10)
1c	0.016 (0.3)	0.030 (3.4)
1d	0.065 (3.4)	0.040 (4.5)
1e	0. (0.0)	0.120 (14)
1b-bis	0.081 (1.7)	0.008 (0.9)
1c-bis	0.032 (0.7)	0.000 (0.0)
1f	0.032 (0.7)	0.043 (4.9)
1g	0.065 (1.4)	0.034 (3.8)
1h	na	0.116 (13)

All reactions were carried out at 100 mM substrate, NAD⁺ 1 mM, sodium phosphate 100 mM, pH 7, 30 °C. na: not assessed. ^a: activity units (U) are defined as μmol of NAD⁺ reduced per minute.

Table S4. BsGlyDH mutations to expand the binding pocket.

Mutations	Distance to NADH (Å)	Solvent accessible area (Å ²)	Activity (U·mg ⁻¹) ^a
WT	-	15418	0.88
V131A	5.20	15430	0.61
Y142A	7.95	15479	0.00
L252A	9.98	15440	0.13
V131A/Y142A	na	15500	0.00
V131A/L252A	na	15452	0.03
Y142A/L252A	na	15503	0.00
V131A/Y142A/L252A	na	15526	0.00

^a Activity with 100 mM glycerol 1 mM NAD⁺ in 100 mM sodium phosphate buffer at pH 7 and 30 °C. Solvent accessible area was calculated using Pymol 0.99v.

Table S5. Gibbs free energies calculated with QM/MM and experimentally determined for different BsGlyDH variants towards different substrates (Table 1).

System	ΔG^\ddagger (kcal·mol ⁻¹) + ZPE corr	$\Delta G^\ddagger_{\text{exp}}$ (kcal·mol ⁻¹)
WT glycerol (Mec 1)	57.6	n.d
WT glycerol (Mec 2)	17.1	16.9
WT S- 1c	18.8	19.2
WT R- 1c	35.6	n.d
L252A glycerol	16.5	16.8
L252A S- 1c	16.2	16.1
L252A R- 1c	44.4	n.d

n.d. Not determined.

Table S6. Immobilization parameters of BsGlyDH-L252A.

Enzyme	Immobilization support	Protein load (mg/g support) ^a	Ψ (%) ^b	Specific immobilised activity (%) ^c	Recovered activity (U/g support) ^d
BsGlyDH-L252A	AG-Co ²⁺	0.62	98	19	5.7 ^e
BsGlyDH-L252A	AG-Co ²⁺	12	99	15	54 ^e

^a Loaded protein to 1 g of carrier after the immobilization process. ^b Immobilization yield, Ψ = (immobilised activity/offered activity) x100. ^c Relative immobilised specific activity (%) is defined as the coefficient between the specific activity of the immobilised enzymes and the specific activity of the soluble ones. ^d Recovered activity of the immobilised enzyme per gram of carrier after the immobilization process. ^e Activity with 100 mM *rac*-**1c**, 1 mM NAD⁺ in 100 mM bicarbonate buffer at pH 9.